universität wien

MASTERARBEIT / MASTER'S THESIS

Titel der Masterarbeit / Title of the Master's Thesis

„Optical Tools for Molecular Quantum Optics“

verfasst von / submitted by

Ksenija Simonović, BSc

angestrebter akademischer Grad / in partial fulfilment of the requirements for the degree of

Master of Science (MSc)

Wien, 2020 / Vienna 2020

Studienkennzahl lt. Studienblatt / degree programme code as it appears on the student record sheet:	UA 066 876
Studienrichtung lt. Studienblatt / degree programme as it appears on the student record sheet:	Masterstudium Physik
Betreut von / Supervisor:	Univ.-Prof. Dr. Markus Arndt
Mitbetreut von / Co-Supervisor:	

Abstract

This thesis demonstrates the development and usefulness of light-based tools, in particular standing light waves, in molecular interferometry. The main result shown is the first experimental realisation of Bragg diffraction of complex, hot molecules in the far-field regime, exhibiting a momentum transfer of up to $18\hbar k$. Demonstrated for a dye molecule phthalocyanine and an antibiotic ciprofloxacin, Bragg diffraction shows promise in becoming a universal beamsplitter for molecular quantum optics. A theoretical overview of far-field diffraction and interactions of molecules with light is followed by a detailed description of the diffraction experiments and obtained results. Bragg diffraction is especially important as a beamsplitter for polar molecules, since material gratings can be used only with limited success due to molecule-grating interactions, subsequent dephasing and loss of interference. The second part of the thesis focuses on a fibre-based beam profiler. Developed and used for alignment in diffraction experiments, it can also be used as a stand-alone tool for measuring laser beams in ultrahigh vacuum and tightly confined spaces.

Zusammenfassung

Die vorliegende Arbeit zeigt die zum ersten Mal realisierte Bragg Beugung organischer Moleküle an einem dicken optischen Lichtgitter. Erfolgreiche Beugung von Farbstoff Phthalocyanin und Antibiotikum Ciprofloxacin betont, dass die Bragg Beugung als Strahlteiler oder Spiegel für polare und polariserbare Moleküle verwendet werden kann. Da solche Moleküle wegen u.a. van der Waals Kräften oft an materiellen Gittern nicht gebeugt werden können, ist die Bragg Beugung ein wichtiger Schritt in Richtung universeller optischer Komponenten für Materiewellenexperimente mit komplexen Molekülen. Die Arbeit umfasst eine theorische Einführung in die Fernfeldbeugung und Wechselwirkung der Moleküle mit Licht, sowie die detaillierte Beschreibung der Bragg Beugung und der durchgeführten Experimente. Anschließend wird ein auf Glasfaser basierter Laserprofiler erläutert, der für Justage in Beugungsexperimenten entwickelt wurde und sich besonders gut für Hochvakuumbedingungen eignet.

Contents

1 Introduction

1.1 Motivation and overview

Ever since de Broglie's seminal hypothesis [1] claiming the wave-like nature of matter by assigning a wavelength $\lambda_{\mathrm{dB}} = h/mv$ to particles of mass m moving with velocity v, matter-waves have become a cornerstone of quantum physics. Experimental demonstrations of the quantum nature of matter and resulting interference of matter waves have, over the past century, been presented for increasingly complex systems, from electrons [2, 3] and neutrons [4, 5] to atoms [6–10], small [11, 12] and complex molecules [13] and even molecular clusters [14]. Furthermore, mass scalability shown by these experiments has made matter-wave physics a powerful tool for numerous sensing and metrology applications and for exploring the limits of the quantum superposition principle for massive particles.

A selection[1] of notable experiments includes fundamental tests measuring gravitational phase shifts and accelerations with neutrons [20] and atoms [21, 22], tests of general relativity and the equivalence principle [23] and measurements of the fine structure constant [24, 25]. The inherent sensitivity of matter-wave interferometers to even minuscule forces allows also for precise measurement of internal molecular properties such as polarizability [26], absolute absorption cross section [27] and ground state diamagnetism [28]. Continuous advances have made it possible to achieve interference of ever more complex and heavier molecules, demonstrating interference of a native polypeptide biomolecule [29] and the current mass record of over 25 thousand atomic mass units [30].

Most of these experiments make use of light-based diffraction elements. Standing light waves are extensively used as phase and diffraction gratings for atoms [31] and molecules [32–34]. Furthermore, coherent beam splitting in atom interferometry has historically been done by making use of single photon recoil [7] or generating entanglement between the atom's electronic and motional state or single photon absorption stimulating Raman transitions [10], achieving a coherent superposition spanning over several millimetres. Nowadays, mainly multi-photon Bragg diffraction [35–37] and Bloch oscillations [38] are used, reliably achieving momentum transfers up to several hundred photon momenta $\hbar k$ [39, 40] and quantum superpositions as large as half a metre [41]. These techniques have, however, not been demonstrated in molecular interferometry, despite the same need for reliable mirrors and beamsplitters.

[1] Comprehensive reviews of atom and molecular interferometry can be found in [15–19].

1.2 Thesis structure

The central result of this thesis is the first experimental demonstration of Bragg diffraction for complex molecules, showing a maximal momentum transfer of 18 $\hbar$k and paving the way towards efficient optical beamsplitters for molecular matter-waves. The thesis begins with a theoretical introduction covering diffraction theory and light-matter interactions (Chapter 2). Next, a detailed description of the experimental setup used (Chapter 3) and a thorough treatment of observed Bragg diffraction (Chapter 4) are given. This includes a theoretical treatment comparing the experiment to simulated predictions and experimental demonstration of diffraction for both polar and non-polar molecules. In addition, Chapter 5 discusses a fibre-based beam profiler developed in the course of Bragg diffraction experiments to measure and monitor the laser grating and its overlap with the molecular beam.

2 Theory

Diffraction phenomena, describing the behaviour of light upon hitting an obstacle or an aperture, were mentioned [42] and later demonstrated in Young's double slit experiment [43]. The mathematical framework commonly used to represent these phenomena, the *Kirchhoff-Fresnel integral* [44], was gradually developed, starting with the integral formulation of Huygens's principle by Fresnel and later ensuring the compatibility with Maxwell's electromagnetic theory of light.

Following that, a matte-wave specific approach via *Wigner functions* [45] was introduced. Defined as a quasi probability function for quantum states in phase space, it provides a useful framework for diffraction phenomena, especially in interferometer configurations. While the Kirchhoff-Fresnel approach calculates the resulting pattern relatively easily, using Wigner functions allows for clearly depicting interactions and propagation between the gratings, influences of the detector, as well as factors such as finite grating or detector size.

The final section focuses on interactions of light with matter. An atom interacting with a light field is modelled as a semiclassical Lorentz oscillator to derive the dynamic complex polarizability. The derived result is then used to analyse interactions of atoms and molecules with an optical diffraction grating.

2.1 Diffraction theory

2.1.1 The Kirchhoff-Fresnel integral

The Kirchhoff-Fresnel integral predicts the propagation of an electric field diffracted at an obstacle, e.g. an aperture, depending on the aperture, the initial field and the geometric setup of the problem, while satisfying the scalar Helmholtz equation. Starting with Maxwell's equations in vacuum and the subsequent wave equation of the electric field

$$\frac{1}{c^2}\frac{\partial^2}{\partial t^2}\vec{E}(\vec{r},t) = \Delta\vec{E}(\vec{r},t) \tag{2.1}$$

the vector Helmholtz equation is obtained by considering a monochromatic wave of the form $\vec{E}(\vec{r},t) = \vec{E}(\vec{r})e^{-i\omega t}$ as

$$\Delta\vec{E}(\vec{r}) + k^2\vec{E}(\vec{r}) = 0, \quad k = \frac{n\omega}{c}. \tag{2.2}$$

Here k is the wave number for propagation in a medium with refraction index n, reducing to $k = \omega/c$ in vacuum. Since the time-dependence is contained only in the exponential factor $e^{-i\omega t}$, it will be left out from now on, as the complete time-dependent field can be obtained by simply

appending said factor to the spatially dependent component. Neglecting the polarisation, the vector equation is simplified to its scalar version

$$\Delta E(\vec{r}) = k^2 E(\vec{r}). \tag{2.3}$$

Under these assumptions, for an aperture placed at $z = z' = 0$ and an incoming field $E(x', y', z') = 0$ (Fig. 2.1), the field at position $E(x, y, z)$ is given by the Kirchhoff-Fresnel integral as [46]

$$E(x, y, z) = -\frac{i}{\lambda} \iint_{\text{aperture}} \mathrm{d}x'\, \mathrm{d}y'\, E(x', y', 0) \cdot \frac{e^{ikR}}{R} \cdot \left[\frac{1 + \cos\left(\vec{R}, \hat{z}\right)}{2} \right] \tag{2.4}$$

where $\vec{R} = (x - x')\hat{\boldsymbol{x}} + (y - y')\hat{\boldsymbol{y}} + z\hat{\boldsymbol{z}}$ is the vector pointing from the aperture's midpoint to the position where the resulting field is calculated and R is the magnitude of $\vec{R}$. For the scalar approximation to maintain its validity, the field should be measured in the distance significantly larger than the wavelength, $R \gg \lambda$ and for small angles, i.e. close to the z-axis. If either of these conditions are violated, the polarisation starts influencing the diffraction significantly and the problem has to be treated with the vector Helmholtz equation (Eq. (2.2)).

The exponential term e^{ikR}/R encodes the Huygens' principle, that is, the superposition of spherical wavelets generated by the incoming field at each point of the aperture. The obliquity factor

$$f_{\text{obl}} = \frac{1 + \cos\left(\vec{R}, \hat{z}\right)}{2} \tag{2.5}$$

ensures that the diffraction occurs mostly in forward direction, reducing to 1 for the field measured on the z-axis and preventing the field from propagating backwards into itself.

Knowing the complex field $E(x, y, z)$, the real valued intensity of the diffraction pattern can be computed as

$$I(x, y, z) = |E(x, y, z)|^2 = EE^*. \tag{2.6}$$

Due to multiplying the field with its complex conjugate, any interference taking place is already encoded within the intensity. Practically, this means that the Kirchhoff-Fresnel approach can be used to analyse and explain phenomena such as diffraction on a slit or a grating or the Poisson spot - a bright spot on axis in the geometric shadow of an object, which can only be explained by diffraction and the wave nature of light.

2.1.2 Near- and far-field diffraction

After passing the diffraction element, the field evolves according to Eq. (2.4). The associated intensity pattern, however, behaves remarkably different depending on the distance from the aperture, leading to the distinction between near- and far-field diffraction. A simplification of the Kirchhoff-Fresnel integral is available for both cases, with the far-field being a limiting case of the near-field. Physically, the difference between the two regimes lies in the influence of the wavefronts' curvature, which is significantly stronger closer to the aperture than at large distances where the wavefronts are nearly parallel.

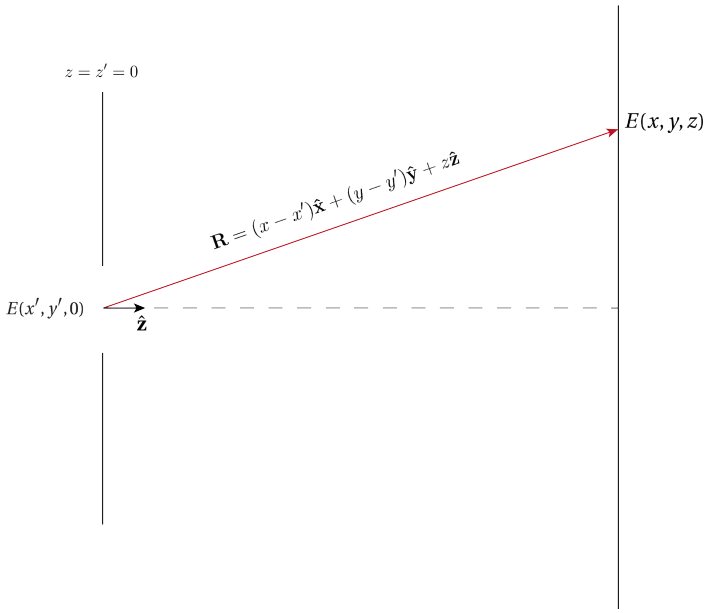

Figure 2.1: For an incoming field $E(x', y', z' = 0)$ arriving at an aperture placed at $z = 0$, the diffracted field at position $\vec{R}$ as measured from the middle of the aperture, $E(x, y, z)$ can be calculated using the Kirchhoff-Fresnel integral [46]. The scalar approximation is valid for fields in large distances compared to light's wavelength and close to the axis defined by the unit vector $\hat{z}$.

The near-field or Fresnel approximation assumes diffraction in the forward direction, setting the obliquity factor (Eq. (2.5)) $f_{\text{obl}} = 1$. This condition is achieved for small angles between $\vec{R}$ and the z-axis and further implies that the field is measured in the distance $R \approx z$ from the aperture. The distance R in the denominator of Eq. (2.4) can hence be approximated as

$$R = z\sqrt{\frac{(x - x')^2 + (y - y')^2}{z^2} + 1} = z\left[1 + \frac{(x - x')^2 + (y - y')^2}{2z^2} + \dots\right]. \tag{2.7}$$

Again, this approximation is performed only in the denominator, as even small changes in the exponential term e^{ikR} could lead to extreme variations in the periodic modulation of the resulting pattern. Substituting this into the integral, the field is given by

$$E_{\text{near}}(x, y, z) = i\frac{e^{ikz}}{\lambda z} \cdot \exp\left[i\frac{k}{2z}(x^2 + y^2)\right] \cdot \iint\limits_{\text{aperture}} \mathrm{d}x'\,\mathrm{d}y'\, E(x', y', 0) \exp\left[i\frac{k}{2z}(x'^2 + y'^2)\right] \cdot \exp\left[-i\frac{k}{z}(xx' + yy')\right]. \tag{2.8}$$

It can be shown that the Fresnel approximation is equivalent to the paraxial approximation in ray optics, as the fields obtained this way are exact solutions to the paraxial wave equation

$$\left[\frac{\partial^2}{\partial x^2} + \frac{\partial^2}{\partial y^2} + 2ik\frac{\partial}{\partial z}\right] E(x, y, z) = 0. \tag{2.9}$$

For a grating with period d, diffraction in the near-field shows the Talbot effect: for the distances z that are integer multiples of the Talbot length

$$L_T = \frac{d^2}{\lambda} \tag{2.10}$$

the obtained pattern is the self image of the grating with the same period. Additional images with smaller periods are found at rational fractions of L_T, termed the fractional Talbot effect. This example shows the defining feature of the near field diffraction pattern, which is that the intensity distribution continually evolves with increasing distance from the aperture. After transitioning to the far field, the pattern only grows in size while maintaining its shape. The transition happens for

$$z \gg \frac{a^2}{\lambda} \tag{2.11}$$

where a is a parameter characterising the aperture size. The first exponential term in the integral in Eq. (2.8) then simplifies to

$$\exp\left[i\frac{k}{2z}(x'^2 + y^2)\right] \approx 1 \tag{2.12}$$

yielding the electric field in far-field or Fraunhofer approximation as

$$\begin{aligned} E_{\text{far}} = -\frac{i}{\lambda z}\exp(ikz) \cdot \exp\left[i\frac{k}{2z}(x^2+y^2)\right] \cdot \\ \cdot \iint\limits_{\text{aperture}} \mathrm{d}x'\,\mathrm{d}y' E(x',y',0)\exp\left[-i\frac{k}{2}(xx'+yy')\right]. \end{aligned} \tag{2.13}$$

The form of the field as defined by the integral does not depend on the distance on z anymore, as changing z influences only the prefactor and scales the intensity in size via the $1/z$, x/z and y/z terms [46]. Figure 2.2 [19] shows the transition from the near- to the far-field for a grating with 10 equidistant slits, with the Talbot self images of the grating on the left hand side transitioning into the constant far-field pattern.

The Kirchhoff-Fresnel formalism can be extended and applied to diffraction of matter-waves as well. Starting with the Schrödinger equation

$$i\hbar\frac{\partial}{\partial t}\psi(t,x) = \left(-\frac{\hbar^2}{2m}\Delta + V(x)\right) = \bar{E}\psi(t,x) \tag{2.14}$$

where $\bar{E}$ represents the total energy and assuming a time-independent potential, an ansatz for the wave function separating the time component can be written as

$$\psi(t,x) \propto \psi(x)\exp\left(-i\frac{\bar{E}t}{\hbar}\right) \tag{2.15}$$

analogously to the monochromatic wave used in the previous derivation. By rewriting the Schrödinger equation as

$$\Delta\psi(x) + k^2\psi(x) = 0 \tag{2.16}$$

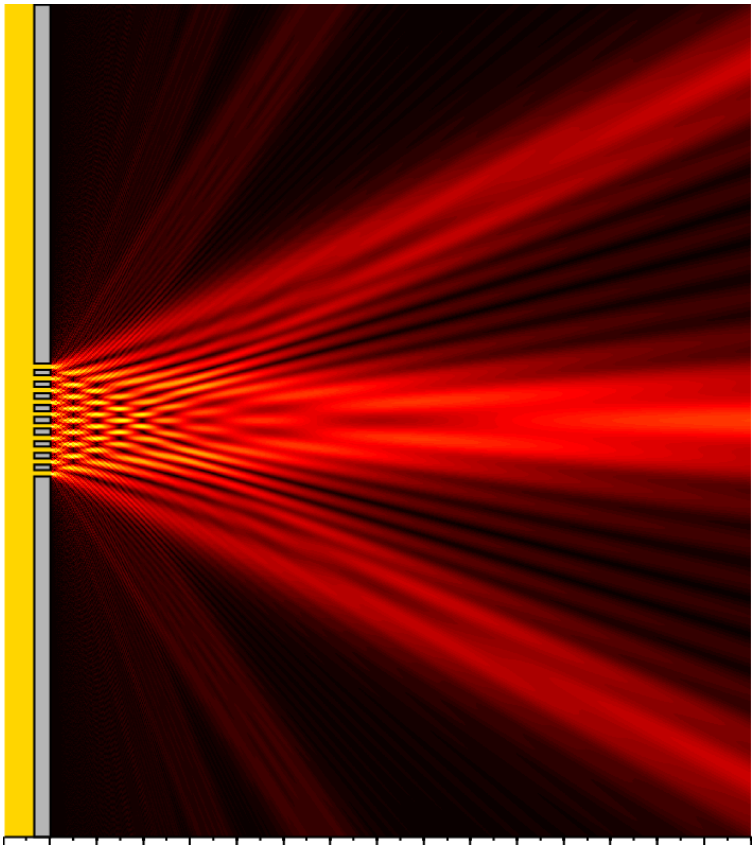

Figure 2.2: Simulation [19] of a grating illuminated by a plane wave showing the diffraction pattern in the near- and far-field. The near-field Talbot carpet, consisting of the repeated self images of the grating on the left hand side transitions into the far-field diffraction pattern on the right. The brightness corresponds to the pattern's intensity at a given spot.

and using the dispersion relation in free space

$$k = \sqrt{\frac{2m}{\hbar^2}(V(x) - \bar{E})} \tag{2.17}$$

it now has the same form as the scalar Helmholtz equation (2.3). The same treatment of the problem as already introduced is now possible as long as the, now position-dependent, dispersion relation is taken into account.

2.2 Wigner functions

Wigner functions [45] are a useful tool for visualising quantum states in phase space. The behaviour of a *single* quantum particle, and in particular, its position and momentum expectation values, can be modelled as behaviour of an *ensemble* of classical particles as governed by statistical mechanics [47, 48]. The defining commutation relation of a quantum phase space with position and momentum coordinates $\hat{x}$, $\hat{p}$ and states $|\psi\rangle$ is

$$\begin{aligned}[\hat{x},\hat{p}] &= i\hbar \\ [\hat{x},\hat{p}]\,|\psi\rangle &= i\hbar\,|\psi\rangle\,.\end{aligned} \tag{2.18}$$

As usual in quantum mechanics, there are two ways for writing out the states $|\psi\rangle$, either as eigenstate decomposition or using the density matrix. For eigenstates $|\alpha\rangle$, the decomposition into a weighted sum

$$|\psi\rangle = \sum_{\alpha} |c_\alpha| e^{i\phi_\alpha}\,|\alpha\rangle \tag{2.19}$$

represents a superposition of basis states, often chosen as plane waves, with their momentum defining the eigenstates continuum. Alternatively, the matrix representation via density operator

$$\rho = |\psi\rangle\langle\psi| \tag{2.20}$$

makes it easier to compute the eigenstates' population and correlations between different eigenstates. The populations are the diagonal elements of the density matrix

$$\rho_{\alpha\alpha} = \langle\alpha|\rho|\alpha\rangle = |\langle\alpha|\psi\rangle|^2 = |c_\alpha|^2 \tag{2.21}$$

The off-diagonal correlations, also called coherences, are computed similarly as

$$\rho_{\alpha\alpha'} = \langle\alpha|\rho|\alpha'\rangle = |c_\alpha c_{\alpha'}| e^{i(\phi_\alpha - \phi_{\alpha'})} \tag{2.22}$$

underlining that coherence is strongly dependent on the eigenstates' phases ϕ_α. The Wigner function can then be defined as a Fourier transform of the density operator in position-space representation and for a transition from the state $|x - s/2\rangle$ to $|x + s/2\rangle$ [48]

$$W(x,p) = \frac{1}{2\pi\hbar}\int_{-\infty}^{+\infty} \mathrm{d}s\, e^{ips/\hbar} \left\langle x - \frac{s}{2}\middle|\rho\middle|x + \frac{s}{2}\right\rangle. \tag{2.23}$$

Equivalently, if the wave function in position space is written as $\psi(x) = \langle x|\psi\rangle$ the Wigner function becomes [49]

$$W(x,p) = \frac{1}{2\pi\hbar}\int_{-\infty}^{+\infty} \mathrm{d}s\, e^{ips/\hbar}\psi^*\left(x - \frac{s}{2}\right)\psi\left(x + \frac{s}{2}\right). \tag{2.24}$$

The Wigner function is a quasi-probability function playing the role of Boltzmann distribution in the classical physics, i.e. providing a probability of a quantum state having a certain position

and momentum. The most important difference compared to classical probability function is that Wigner function can take negative values as well, which are an unmistakable characterisation of quantum states. Probability distribution functions with respect to either position or momentum, i.e. the distribution's marginals, can be extracted[2] from the Wigner function as

$$\begin{aligned} W_{\mathsf{pos}}(x) &= \frac{1}{2\pi\hbar}\int_{-\infty}^{+\infty} \mathrm{d}p\, W(x,p) = \langle x|\rho|x\rangle \\ W_{\mathsf{mom}}(p) &= \frac{1}{2\pi\hbar}\int_{-\infty}^{+\infty} \mathrm{d}x\, W(x,p) = \langle p|\rho|p\rangle\,. \end{aligned} \tag{2.25}$$

Over the entire phase space, the Wigner function integrates to unity

$$\iint_{-\infty}^{+\infty} \mathrm{d}x\,\mathrm{d}p\, W(x,p) = 1 \tag{2.26}$$

since both the position and momentum have to be found somewhere within the configuration phase space.

More generally, the Wigner function is a part of the Wigner-Weyl transform, an invertible mapping between position representation operators in the Schrödinger picture and their phase space equivalents [50]. A Wigner transform brings a general operator $\hat{A}$ from position representation into phase space as

$$A(x,p) = \int_{-\infty}^{+\infty} \mathrm{d}s\, e^{ips/\hbar} \left\langle x - \frac{s}{2}\middle|\hat{A}\middle|x + \frac{s}{2}\right\rangle \tag{2.27}$$

while the inverse, the Weyl transform, maps an operator from the phase space to the position representation.

Wigner functions are especially useful for describing diffraction and interference, and consequently interferometers. This approach is scattering-based, alternating between free propagation and interacting with diffraction elements, making it well-suited for thin-grating interferometers. While this makes it less applicable to thick Bragg diffraction gratings used in this work, the formalism gives a good general overview of interactions with light-based gratings and is included for the sake of completeness. Starting with a Wigner function $W_0(x,p)$ of a particle with mass m, the free evolution in time t is obtained by a shearing transformation

$$W_t(x,p) = W_0\left(x - \frac{tp}{m},\, p\right). \tag{2.28}$$

Transmission through a grating is given as a convolution of an incoming[3] Wigner function W_0

[2] See [48] for a detailed calculation.

[3] Since we are, at this point, only interested in the transmission through the grating, the incoming function is again denoted by W_0. For a more complete treatment where the propagation in front of the grating plays a role, $W_0 = W_t(x,p)$ as defined by Eq. (2.28) is implied.

with the transmission kernel $T(x,p)$

$$W'(x,p) = \int \mathrm{d}r\, W_0(x,r)T(x,\, p-r) \tag{2.29}$$

The transmission kernel has the form

$$T(x,p) = \frac{1}{2\pi\hbar}\int \mathrm{d}s\, e^{ips/\hbar} t\left(x-\frac{s}{2}\right) t^*\left(x+\frac{s}{2}\right) \tag{2.30}$$

where $t(x)$ is the transmission function changing the incoming wave function $\psi(x) = \langle x|\psi\rangle$ to

$$\psi'(x') = t(x)\psi(x). \tag{2.31}$$

depending on the position x at the grating at which the transmission occurs, the interaction potential with the grating V and the forward momentum $p_z \equiv p$ as

$$t(x) = \left|\tilde{t}(x)\right| \exp\left[-i\frac{m}{p\hbar}\int \mathrm{d}z V(x,z)\right]. \tag{2.32}$$

The spatial coefficients $\tilde{t}(x)$ can be determined using a Fourier series decomposition, as detailed in [51]. For the case of a thin optical grating of period $d = \lambda/2$ formed by a standing light wave, the final amplitude transmission function can be written as

$$t(x) = \exp\left[\left(-\frac{n_0}{2} + i\phi_0\right)\cos^2\left(\pi\frac{x}{d}\right)\right]. \tag{2.33}$$

The parameters ϕ_0 and n_0 (Eq. (2.52), (2.56)) are the maximal phase shift imprinted on molecules when passing through the grating and the maximal number of absorbed photons in the grating's antinode, respectively.

2.3 Matter-light interactions

Depending on the phenomena of interest, interactions of matter with light can be described in several different frameworks. Einstein's rate equations, for instance, describe classical dynamics of absorption, stimulated and spontaneous emission of radiation for a classical light-field and a quantized atom, while the optical Bloch equations develop a quantum perturbation theory under the same conditions, describing the full coherent evolution for the case of intense light. A full quantum treatment, on the other hand, is provided by the Jaynes-Cummings model, taking into account interactions of a quantized atom with a likewise quantized electric field. This approach always provides a coherent evolution, but is mostly used in cases where matter interacts with only a few photons.

2.3.1 Lorentz model

Atom-light interactions can be described classically by modelling an atom as a damped harmonic oscillator with a single electron bound to the nucleus, in what is known as the Lorentz model and summarised[4] here. An atom in this picture has a single oscillating electron driven by a

[4] See [52, 53] for a more detailed description.

monochromatic time-dependent electric field associated with light of wavelength λ

$$\vec{E}(t) = \hat{\varepsilon} E_0 e^{-i\omega t} \tag{2.34}$$

with the unit vector $\hat{\varepsilon}$ and $\omega = 2\pi c/\lambda$ describing the polarisation and the frequency of the light field respectively. This classical model is a good approximation for small electron displacements and, more generally, for cases well-described by harmonic potentials. Furthermore, the model helps to develop a clear intuition about polarizability depending on the driving frequency, the atom's resonant frequency, and possible detuning.

In the dipole approximation, i.e. assuming that the wavelength is a lot longer than the atom's diameter, the variations of $\vec{E}$ across the atom are negligible. The force exerted on the electron carrying charge e can then be written as

$$\vec{F} = -e\vec{E} = -eE_0 e^{-i\omega t}\hat{\varepsilon}. \tag{2.35}$$

On the whole, the electron satisfies the equation of motion

$$m\frac{\mathrm{d}^2\vec{x}}{\mathrm{d}t^2} + \gamma m\frac{\mathrm{d}\vec{x}}{\mathrm{d}t} + \omega_0^2\vec{x} = -eE_0 e^{-i\omega t}\hat{\varepsilon} \tag{2.36}$$

written in the centre-of-mass system for a resonant oscillation frequency ω_0 with reduced mass

$$m = \frac{m_n m_e}{m_n + m_e} \approx m_e \tag{2.37}$$

since the nucleus' mass m_n is singificantly larger than the electron mass m_e. The damping or friction term $\gamma m\frac{\mathrm{d}\vec{x}}{\mathrm{d}t}$ models radiative losses due to charge acceleration or collisions with other nearby atoms. In the quantum picture, looking at an isolated atom as a two-level system [54], the coefficient γ equals the Einstein's A_{21} coefficient describing the spontaneous decay of the excited into the ground state

$$\gamma = A_{21} = \frac{1}{\tau} = \frac{|M_{12}|^2\omega_0^3}{3\pi\varepsilon_0\hbar c^3}. \tag{2.38}$$

Here τ is the lifetime of the excited state and $|M_{12}|$ is the dipole matrix element governing the transition between the states $|1\rangle$ and $|2\rangle$.

Assuming that the averaged electron's position $\vec{x}$ follows the electric field (Eq. (2.34)), an ansatz can be written as

$$\vec{x}(t) = \hat{\varepsilon} x_0 e^{-i\omega t}. \tag{2.39}$$

Eq. (2.36) is then solved for

$$x_0 = \frac{eE_0}{m}\cdot\frac{1}{\omega^2 - \omega_0^2 + i\gamma\omega} = x_0(\omega) \tag{2.40}$$

with complex Lorentzian dependence on the driving field frequency ω. Knowing the average position $\vec{x}$ and the electron's dipole moment $\vec{q} = -e\vec{x}$, the polarizability $\alpha(\omega)$ is defined to measure how easily the field $\vec{E}$ induces that dipole moment:

$$\vec{q} = \alpha(\omega)\vec{E} \tag{2.41}$$

and is given by

$$\alpha(\omega) = \frac{e^2}{m} \cdot \frac{1}{\omega_0^2 - \omega^2 - i\gamma\omega}. \tag{2.42}$$

The polarizability is a complex quantity, describing the atom's response to the applied electric field in full. As such and given in the frequency space, the response can also be understood as a Fourier transform of the applied field. The real part $\mathrm{Re}(\alpha)$ describes scattering processes, while the imaginary part $\mathrm{Im}(\alpha)$ describes absorption of radiation. Furthermore, $\mathrm{Re}(\alpha)$ is a Lorentzian curve with full width half maximum (FWHM) of γ, corresponding to the reciprocal excited state's lifetime (Eq. (2.38)) as illustrated in Fig. 2.3.

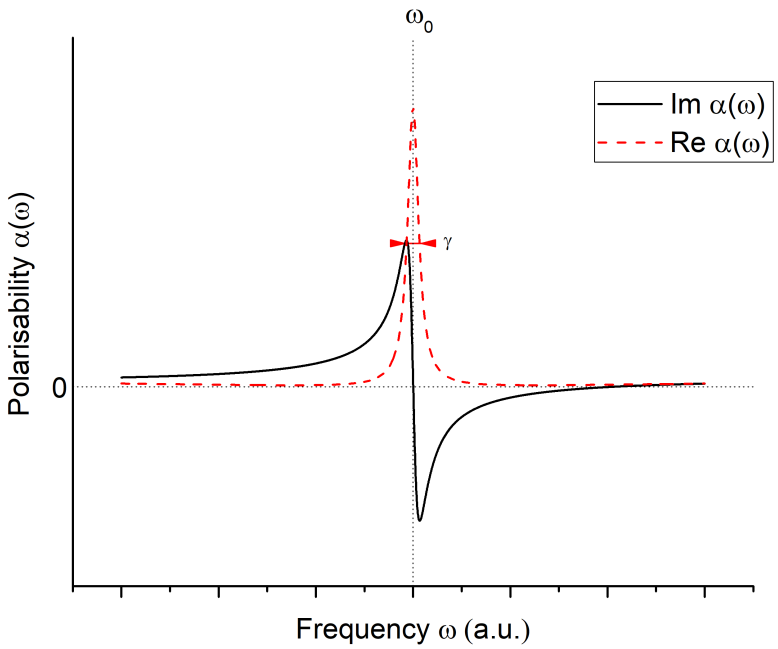

Figure 2.3: Complex polarizability $\alpha(\omega)$ for an atom in an electric field at and around resonance ω_0. The real part (red dashed curve) is a Lorentzian curve describing scattering processes with full width at half maximum γ and reaching its maximum at the resonance. The imaginary part (black solid curve) describes the absorption of radiation by the atom.

If an atom has several electrons or different possible transitions k the polarizability becomes

$$\alpha(\omega) = \frac{e^2}{m} \sum_k f_{0k} \frac{1}{\omega_{0k}^2 - \omega^2 - i\gamma_k\omega} \tag{2.43}$$

where all contributions of single electrons (Eq. 2.42) are weighted and summed up. The weighing factor f_{0k}, also called the oscillator strength factor, is dimensionless and describes the fraction of the total energy (in the classical case) belonging to a particular transition [55]. Moreover, it

describes the ratio between quantum and classical absorption cross section as

$$f_{0k} = \frac{\sigma_{0k}}{\sigma_{\text{classical}}} = \frac{2\pi m \varepsilon_0 c^3}{e^2} \cdot \frac{\gamma_k}{\omega_{0k}^2} \tag{2.44}$$

with

$$\sum_k f_{0k} = 1. \tag{2.45}$$

The sum condition, known as the Thomas-Reide-Kuhn rule, follows directly from the fact that the oscillator strengths describe fractions of the total classical energy. Subscript k indicates that the quantity is specific to the kth transition or electron, with the zero showing that all of them originate from the ground state. More generally, for transitions between two states j, k, one can write

$$f_{jk} \cdot g_j = -g_k \cdot f_{kj} \tag{2.46}$$

with $g_{j,k}$ representing the corresponding states' degeneracy factors [55]. For degenerate energy states, the oscillator strength then represents an average over all magnetic quantum numbers of those states.

2.3.2 Interactions of matter with a standing light-wave

In most experiments making use of optical gratings, these gratings are standing light waves, built by retroreflecting a laser beam back into itself. For a Gaussian beam propagating along the x-axis (see Section 5.1 for a detailed mathematical description) the time-averaged intensity profile is

$$I(x, y, z) = \frac{8P}{\pi w_y w_z} \cdot \exp\left[-2\left(\frac{y^2}{w_y^2} + \frac{z^2}{w_z^2}\right)\right] \cdot \cos^2\left(\pi \frac{x}{d}\right) \tag{2.47}$$

and directly proportional to the squared intensity of the associated electric field $\vec{E}$, $E = |\vec{E}|$

$$I = \frac{1}{2} c \varepsilon_0 E^2. \tag{2.48}$$

In Eq. (2.47) P is the laser power, $w_{y,z}$ are the beam waists along the x- and z-axis and $k = 2\pi/\lambda$ is the magnitude of the wave vector. The period of the grating, $d = \lambda/2$, is half of the laser's wavelength. When a particle with polarizability α passes through a light-grating, a dipole moment $\vec{q} = \alpha \vec{E}$ is induced and the particle experiences a potential

$$V = -\vec{d} \cdot \vec{E} = -\frac{1}{2} \alpha E^2 = -\frac{\alpha}{c \varepsilon_0} I \tag{2.49}$$

Depending on its position in this potential the particle's phase is shifted by [51]

$$\Delta\phi(x) = -\frac{1}{\hbar} \int_{-\infty}^{+\infty} \mathrm{d}t \, V = \frac{\alpha}{c \varepsilon_0 \hbar} \int_{-\infty}^{+\infty} \mathrm{d}t \, I(x, y, z, t). \tag{2.50}$$

The integration is done using the eikonal approximation [51, 56], assuming the trajectory of the particle remains unaffected by the laser grating during the interaction. The spatial coordinate in

flight direction z can then be expressed in terms of velocity and transit time as $z = v_z t$, resulting in

$$\Delta\phi(x) = \phi_0 \cos^2\left(\pi \frac{x}{d}\right). \tag{2.51}$$

The maximal phase shift is obtained when the cosine equals 1 and is

$$\phi_0 = \Delta\phi_{\mathsf{max}} = \sqrt{\frac{2}{\pi}} \cdot \frac{\alpha}{\hbar c \varepsilon_0} \cdot \frac{P}{w_y v_z}. \tag{2.52}$$

Additionally, a particle may absorb several grating photons while traversing the light field. Assuming that individual absorption events are independent from each other, the probability P_n of absorbing n photons can be modelled via Poisson distribution

$$P_n(n_0) = n_0^n \frac{e^{-n_0}}{n!}. \tag{2.53}$$

The local photon absorption rate Γ depends only on the laser intensity and the absorption cross section

$$\sigma_{\mathsf{abs}} = \frac{2\pi}{\varepsilon_0 \lambda} \operatorname{Im}(\alpha) \tag{2.54}$$

and is given by

$$\Gamma(x, z) = \frac{\lambda}{hc} I(x, z) \sigma_{\mathsf{abs}}. \tag{2.55}$$

The position-dependent number of absorbed photons is obtained by integrating along the particle's path [51] as

$$\begin{aligned} n(x) &= \int_{-\infty}^{+\infty} \mathrm{d}t\, \Gamma(x, z = v_z t) = n_0 \cos^2\left(\pi \frac{x}{d}\right) \\ n_0 &= \frac{8}{\sqrt{2\pi}} \cdot \frac{\sigma_{\mathsf{abs}} \lambda}{hc} \cdot \frac{P}{w_y v_z} \end{aligned} \tag{2.56}$$

where n_0 is both the maximal possible number of absorbed photons and the mean number of photons absorbed in the grating's antinode. Knowing this and the maximal phase shift ϕ_0 (Eq. (2.52)), a dimensionless parameter characterising the grating can be defined as

$$\beta = \frac{1}{4\pi\varepsilon_0} \cdot \frac{n_0}{4\phi_0} = \frac{\sigma_{\mathsf{abs}} \lambda}{8\pi^2 \alpha} \tag{2.57}$$

For $\beta \gg 1$ the phase shift is negligible and the grating acts as a purely absorptive one, while it is a pure phase grating for $\beta \ll 1$.

2.3.3 Behaviour of atoms and molecules

In principle, the discussion presented here, especially the frequency-dependent behaviour of polarizability (Eq. (2.42)), can be applied to molecules, too. The problem, however, lies in the exceedingly complex internal structure of molecules compared to single atoms. Since the molecular internal states are close together, it can be hard to address only a particular transition. This is further complicated by broad molecular spectral lines[5], often orders of magnitude broader than their atomic counterparts.

Absorption of photons presents an additional issue in matter-wave experiments [57, 58]. Depending on specific parameters and molecules used, absorption can lead to depletion of the beam via ionisation or fragmentation. Additionally, heating of the molecules and reemission of an absorbed photon can in some cases lead to decoherence and subsequent loss of the interference pattern [59, 60].

[5] See Fig. 3.5 and 3.6 for an illustration of this and the spectra of molecules used in the experiment.

3 Experimental setup

The far-field diffraction apparatus used in this work consists of three main components: the laser desorption stage, the interference chamber and the fluorescence microscope. Its main advantage lies in its versatility and relatively easy alignment compared to multi-grating interferometers. This allows for numerous different experiments and a sandbox environment for testing new sources, beamsplitters and detection methods. Examples of previous work done in this setup include investigating the influence of molecular dipole moments [61] and van der Waals interactions with the grating walls on the interference pattern [62], demonstrating a diffraction grating made out of single-layer graphene [63] and quantum interference at the skeleton of an alga [64].

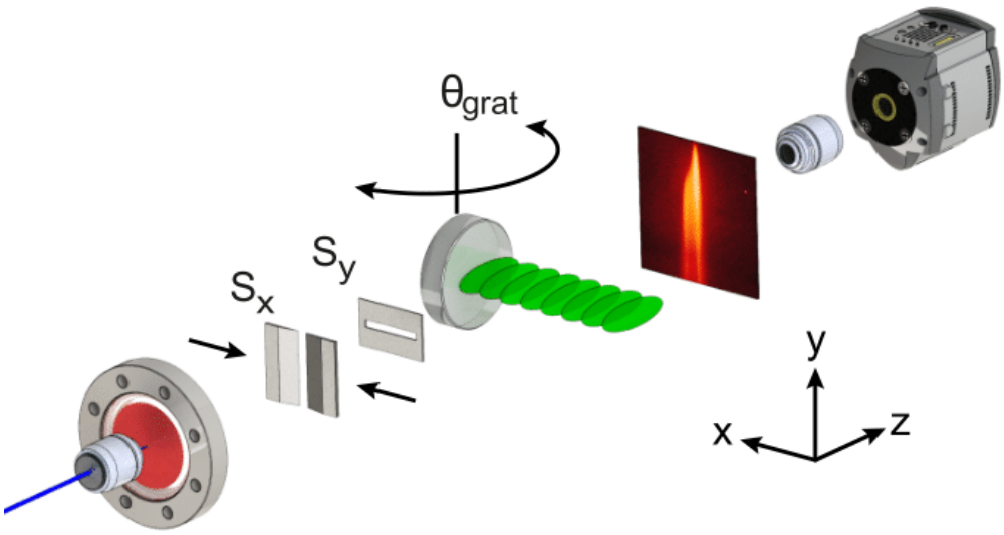

Figure 3.1: Schematic overview of the far-field diffraction apparatus used for Bragg diffraction experiments [65]. A coherent molecular beam is generated via microfocused laser desorption, collimated horizontally and vertically using the slits S_x and S_y and diffracted at a grating, here formed by a standing light wave. The resulting pattern is imaged using fluorescence microscopy.

The diffraction apparatus' principle is illustrated in Fig. 3.1 and can be summarised as follows: A coherent molecular beam is generated by tightly focusing a laser beam onto a thin sample surface, so that the sample is sublimated. The beam is collimated using horizontal and vertical slits and diffracted at a standing light wave after 1.5 m of free flight. After passing the grating, the molecules are collected on a 170 µm thin quartz plate further 0.57 m downstream, where they are imaged via laser-induced fluorescence microscopy. All diffraction experiments were done in vacuum at or below 1×10^{-8} mbar to prevent unwanted interactions, reduce possible environmental effects and minimise collisions with the residual gas which could lead to signal

depletion or decoherence. The setup is evacuated by a series of turbomolecular pumps with the total nitrogen pumping capacity of 1275 l/s and the pressures of the source, interferometer and detection chamber independently monitored. The following sections give a detailed view of all stages and their operation, as well as the molecules used in the experiment and their properties.

3.1 Molecular source

A stable, coherent beam of molecules is generated by focused laser desorption, as illustrated in Fig. 3.2.

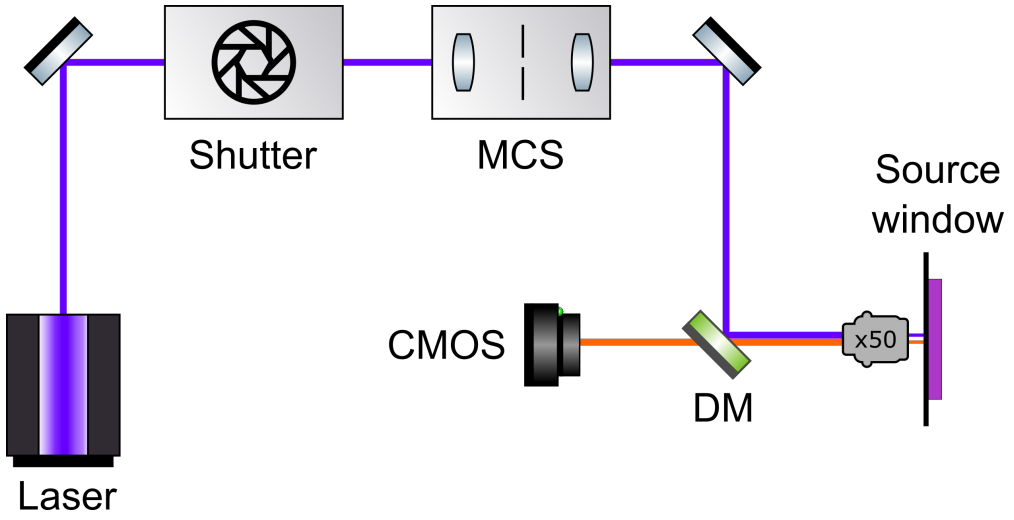

Figure 3.2: Schematic overview [66] of the desorption scheme generating a molecular beam. A beam from a blue laser diode at 420 nm passes a mechanical shutter and a mode cleaning stage **MCS** before being reflected on a dichroic mirror **DM** and focused to roughly a micrometer-large spot on the inside of a vacuum window. Here it is absorbed by a thin film of molecules which are evaporated from the surface and follow a Maxwell-Boltzmann velocity distribution. A continuous stream of molecules is obtained by moving the window via a motorised two-dimensional translation stage. Fluorescence emitted by desorbed molecules (represented by an orange beam) is transmitted back through the objective and **DM** and registered on a CMOS camera to monitor the focus.

A 420 nm blue laser diode passes a mechanical shutter and a mode cleaning stage **MCS** consisting of two lenses and a pinhole between them, ensuring that everything but the Gaussian TEM_{00} mode is filtered out. The beam is then reflected on a dichroic mirror **DM** and focused by a x50 magnifying objective to a $1.6(1)$ µm spot onto the inside of the source vacuum window, covered with a thin layer of prepared molecules. The molecules on the inside of the window sublimate when heated, following a roughly Maxwell-Boltzmann velocity distribution To obtain a constant stream of molecules, the source window is moved using a VAB motorised two-dimensional translation stage.

The significance of the tight laser focus is twofold. Firstly, it ensures that the molecules are heated and evaporated only locally, without inducing possible thermal damage to the rest of the

layer. Secondly, a small effective source size helps achieve sufficient transverse coherence of the beam, defined as

$$X_c = \frac{2\lambda_{\mathrm{dB}} L}{s}. \tag{3.1}$$

The transverse coherence width quantifies the portion of the grating that can be illuminated coherently in distance L from a source of size[6] s producing molecules with de Broglie wavelength λ_{dB}. For a molecule[7] of mass 514 u flying at 250 m/s, the coherence width at the position of the grating is 5.8 µm, illuminating 22 diffraction periods of 266 nm length coherently.

The focus is monitored by observing the fluorescence light emitted by the excited molecules, which is transmitted through the objective and the dichroic mirror onto a CMOS sensor. The objective is mounted on a micrometer translation stage, allowing for fine-tuning of the focus. Furthermore, to ensure a consistent beam generation, the tilt angle of the vacuum window is adjusted so that the beam is hitting the window perpendicularly. To exclude fragmentation of molecules during desorption, molecules were collected on a glass microscope slide after a centimetre of free flight and the sample subjected to a spectroscopy analysis [65, 67]. Matrix-assisted laser desorption/ionisation shows that over 99% of the sample is desorbed without thermally induced fragmentation or other thermal damage.

All experiments presented here have been done using a so-called dropped source. Such sources are prepared by dissolving a molecular sample in acetone to obtain a moderately thick solution, which is then spread on the inner surface of the vacuum window and left to dry. An alternative is presented by evaporated sources, where a laser desorption mechanism similar to the one described here is employed to deposit molecules from a dropped source onto another window where they condense again to form a thin uniform layer. This window is then used as a source window in the experiment. Evaporated sources show considerably larger transverse coherence due to the high homogeneity and minimal thickness of the molecular layer, but the trade-off involves a significantly lower molecular flux, increasing the experiment duration.

3.2 Diffraction grating

The grating for Bragg diffraction experiments was formed by retroreflecting a 532 nm laser beam (Coherent Verdi V-18) to form a standing light wave, as illustrated in Fig. 3.3. The orientation of the light grating with respect to the molecular beam and the coordinate axes used in further text are the same as introduced in the schematic overview in Fig. 3.1. The coherence length of the laser can be estimated using the manufacturer specified frequency stability as

$$L_c = \frac{c}{\Delta\nu} = \frac{\lambda^2}{\Delta\lambda} \tag{3.2}$$

and amounts to 59.8 m for $\Delta\nu = 5$ MHz. Longitudinal coherence describes the phase relations along the direction of the wave propagation, so that two waves from the same source with a

[6] Here the source size is given by the size of the laser focus, $s = 1.6(1)$ µm.
[7] Phthalocyanine as used in the experiments, see Section 3.3 for detailed properties.

slight difference in wavelength or frequency completely dephase over $L_c/2$ and are back in phase after L_c. As the distances in the experiment are on the order of several meters, the phase of the standing light wave can be taken as constant.

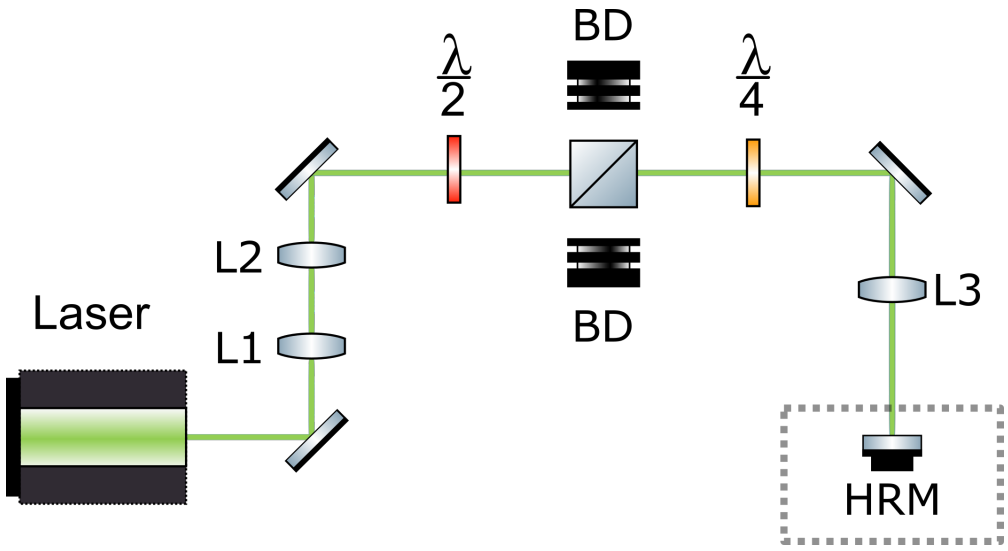

Figure 3.3: Sketch [66] of the scheme generating the optical standing light wave grating used in Bragg diffraction experiments. A 532 nm laser beam is expanded horizontally by a telescope consisting of spherical lenses **L1** and **L2**, passes a half-wave plate $\boldsymbol{\lambda/2}$, a polarising beamsplitter cube and a quarter-wave plate $\boldsymbol{\lambda/4}$. The cylindrical lens **L3** focuses the beam vertically before entering the vacuum chamber, indicated by a gray dashed rectangle. The standing light wave is formed by reflecting the beam back into itself from a highly reflective mirror **HRM**, whose angle and position can be controlled with µrad precision. The half- and quarter-wave plates are used to, respectively, vary the grating power and redirect the reflected beam to beam dumps **BD**, to avoid damage to the laser.

The beam is expanded to a horizontal waist of $w_z = 7.04(6)$ mm using a telescope formed by plano-convex lenses **L1** and **L2** with focal lengths of 40 mm and 250 mm respectively. After passing a half-wave plate $\boldsymbol{\lambda/2}$, a polarising beamsplitter cube and a quarter-wave plate $\boldsymbol{\lambda/4}$, the beam is directed to a cylindrical lens **L3** with 250 mm focal length, whose position and orientation determine the vertical grating waist w_y of 55–65 µm. The grating is formed by reflecting the incoming beam off of a highly reflective mirror **HRM** inside the vacuum chamber (grey dashed box in Fig. 3.3) back into itself. To avoid damage to the laser by the reflected beam, the quarter-wave plate $\boldsymbol{\lambda/4}$ is set to redirect the reflected beam into the beam dumps **BD** on the side of the beamsplitter cube.

The mirror is controlled using a custom-made holder coupled to a SmarAct linear stage with 26 mm motion range at 1 nm step size and a piezosystem jena PSH10/2 piezo-based tilt system varying the mirror's angle about the y- and z-axes with 0.2 µrad precision within a 8 mrad range. While the laser was, for stability reasons, always operated in high-power mode, i.e. at maximal output power of 18 W, the actual power of the grating was varied via the half-wave plate $\boldsymbol{\lambda/2}$ and measured in front of the vacuum chamber, assuming no significant losses in

transmission through the chamber window. To ensure thermal stability of the laser and the mirror holder, the laser was left to run through the setup at high power for three to four hours before each experimental run.

3.3 Molecules and detection

3.3.1 Molecular properties

The molecules used for diffraction experiments were a dye molecule phthalocyanine[8] and an antibiotic ciprofloxacin, both illustrated in Fig. 3.4. The molecular properties relevant for the experiments - mass, dipole moment, polarizability quantified via static polarizability volume and the absorption cross section - are listed in Table 3.1.

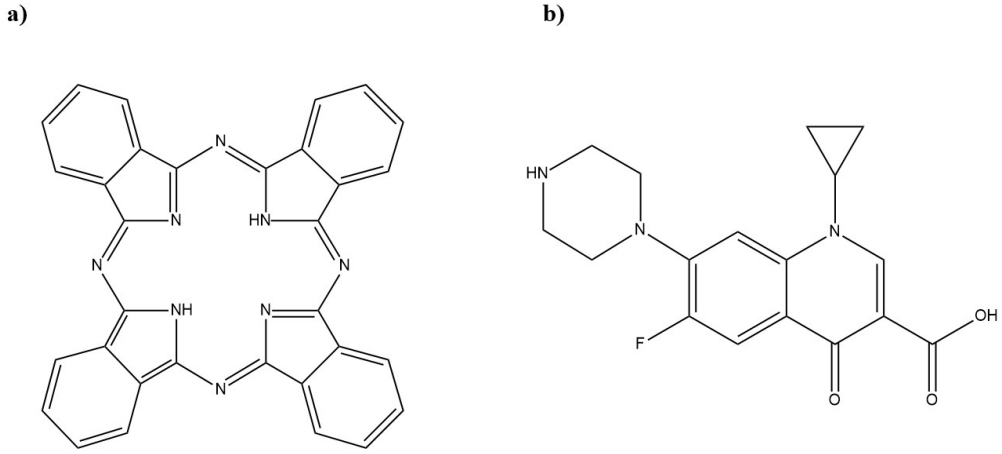

Figure 3.4: Structural formulae of **a)** the nonpolar dye molecule phthalocyanine and **b)** the polar antibiotic ciprofloxacin used in presented diffraction experiments.

Table 3.1: Experimentally relevant properties of phthalocyanine and ciprofloxacin.

Property	Phthalocyanine	Ciprofloxacin
Mass (amu)	515	331
Dipole moment (Debye)	nonpolar	2.67 [68]
Polarizability volume at 532 nm ($Å^3$)	101 [69]	38.9
Absorption cross section at 532 nm (cm^2)	9×10^{-18} [70]	$\ll 10^{-18}$ [71]

Absorption and fluorescence spectra of both molecules are shown in Fig. Fig. 3.5 for ciprofloxacin and Fig. 3.6 for PcH_2 respectively.

[8] Abbreviated PcH_2.

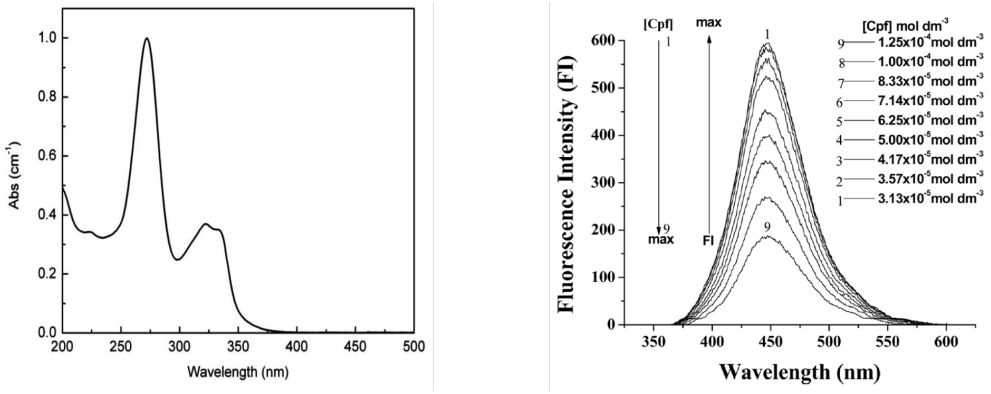

Figure 3.5: Absorption (left, [72]) and fluorescence (right, [73]) spectra of ciprofloxacin in aqueous solutions. The maximal fluorescence intensity is measured at around 450 nm for several different concentrations.

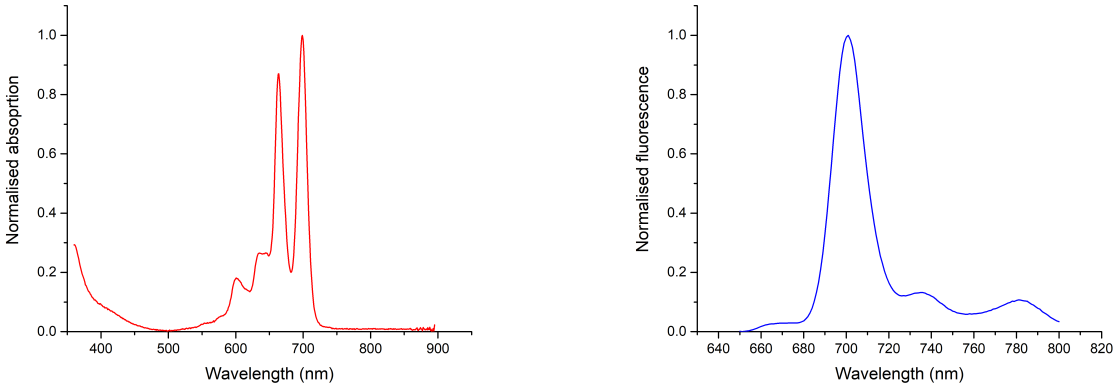

Figure 3.6: Normalised absorption (left) and fluorescence (right) spectra of phthalocyanine, measured in chloronaphthalene solutions [70].

Notably, PcH_2 has a significantly higher polarizability and absorption cross section, allowing for studying of photon absorption in the grating and its possible influence on the diffraction pattern.

3.3.2 Detection

Interference patterns are imaged using laser-induced fluorescence microscopy [74]. After passing the diffraction grating, molecules are collected on a thin quartz plate and illuminated by a flat-top laser beam. The emitted fluorescence is collected by a 20-fold microscope objective (ZEISS PLANNEO FLUAR, numerical aperture 0.5) and recorded using an electron multiplying CCD camera (ANDOR IXON DV885 - K(S-VP)). Repeated deposition and imaging is made possible by *in situ* plasma cleaning. To this end, the detection chamber is separated from the rest of the setup and flushed with air or nitrogen through a needle valve to reach the 1–4 mbar pressure range. By placing a 0.5 mm thin electrode close to the outside of the detection window and applying a 1.5 kV, 10 kHz AC voltage, the gas inside the chamber is ignited to a plasma, while

the grounded vacuum chamber serves as a counter electrode. The plasma removes the molecules gathered on the quartz plate, presumably so that they are burned off and pumped out of the chamber or left to form an amorphous carbohydrate layer coating the chamber walls. Either way, the accumulated molecules are effectively removed from the plate and the operation can be resumed as soon as the pressure drops back to the 10^{-8} mbar range. This takes roughly an hour if the chamber is flushed with air, less if nitrogen is used.

To separate the fluorescence signal from the background, the detection laser and the grating laser, bandpass filters in the 700–725 nm range for PcH_2 and 500–595 nm for ciprofloxacin were used. PcH_2 was illuminated with about 30 mW of red 661 nm light, very close to its second-highest absorption maximum at 664 nm (see Fig. 3.6). Strong excitation and fluorescence produce consistently high signal with good signal-to-noise ratio. Previous experiments have demonstrated that each molecule can be localised with precision better than 10 nm, allowing for real-time imaging of single molecules and the accumulation of the diffraction pattern [74, 75].

For the detection of ciprofloxacin, in this thesis we switch from 420 nm [76] to 266 nm illumination, close to an absorption maximum at approximately 272 nm (Fig. 3.5). The UV beam was generated by frequency doubling a 532 nm laser beam (Coherent Verdi V-10) in an external resonator (Sirah WaveTrain 2), resulting in about 100 mW of UV power when pumping the resonator with 3.66 W. To compare the two illumination wavelengths, a wide stripe of ciprofloxacin was deposited onto the quartz plate and imaged with both, while keeping all the other parameters constant. The camera images with 20 s integration time and an EM gain of 1, together with vertically summed traces, are compared in Fig. 3.7, with the dashed line indicating the regions summed over. The maximal signal, at the stripe borders, increases by a factor of 5 upon switching to 266 nm. Furthermore, the signal fluctuations are significantly lower, especially visible in the middle of the stripe where the 266 nm illumination produces a virtually constant signal, consequently improving the signal-to-noise ratio. While this illumination produces significantly better images, care should be taken about possible bleaching of molecules on the surface preventing further fluorescence if repeated imaging of the same pattern should be required. All images presented in this work were taken, at the longest, over the course of an hour and illuminated up to 6 times with the pattern remaining stable during the process.

3.4 Alignment

Due to Bragg diffraction's pronounced angular dependence, alignment is critically important. This section covers the alignment of the molecular beam and the laser grating, together with details on how to align both respectively to each other for optimal diffraction results.

3.4.1 Alignment of the molecular beam

Horizontal alignment of the molecular beam in the xz-plane (see Fig. 3.1, 3.8 for the coordinate system's orientation) ensures a straight-line transmission from the source to the detector parallel to the chosen flight axis and effective collimation, cutting the molecular beam symmetrically along

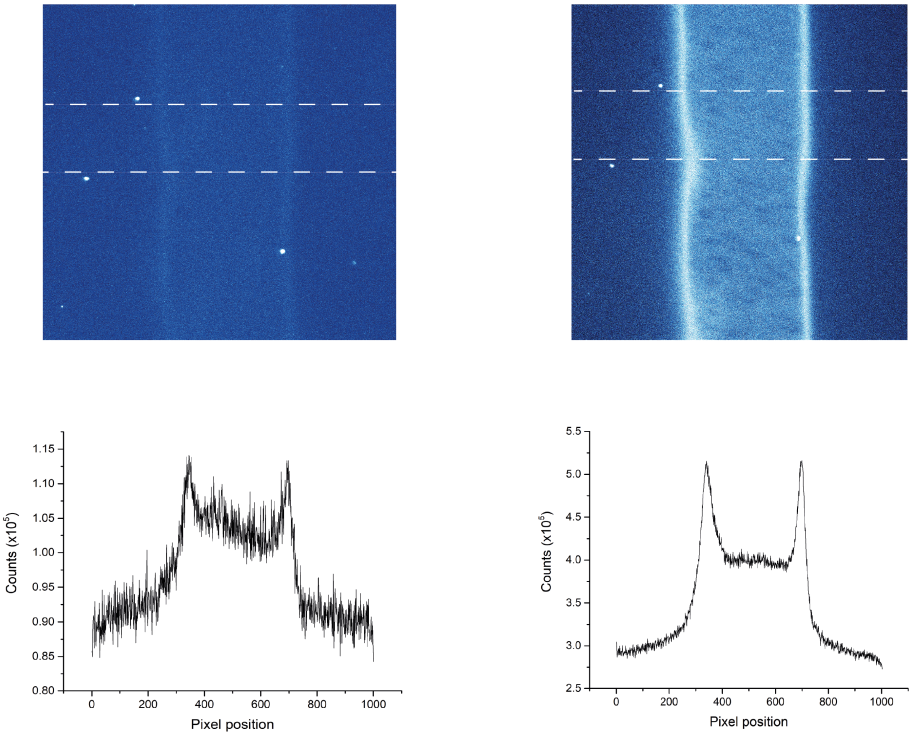

Figure 3.7: Comparison of ciprofloxacin images taken with roughly 100 mW illumination at 420 nm (left) and 266 nm (right). Vertically summed traces plot the number of registered counts against the pixel position. The dashed line in above images indicates the region from which the below traces are taken. Both images are taken with 20 s exposure and integration time and an EM gain of 1 in the 500–595 nm wavelength range.

the z-axis. The alignment, illustrated in Fig. 3.8, is done by varying the source's position on the x-axis and alternatively narrowing the piezo-controlled collimation slits $\mathbf{S_1X}$ and $\mathbf{S_2X}$ (maximally 210 µm and 150 µm wide, respectively) until both transmitted stripes are centred around the same position on the detector with 1.6 µm or better precision. During the final diffraction experiments, $\mathbf{S_1X}$ is left completely open and the beam is collimated by $\mathbf{S_2X}$, corresponding to the slit $\mathbf{S_x}$ in Fig. 3.1. While using a single slit is sufficient for collimation, aligning with both slits ensures the desired straight-line transmission and reduces any possible effects of source broadening.

3.4.2 Laser grating and diffraction

The next step is the generation and alignment of the laser grating. First, the beam focused by the cylinder lens (**L3** in Fig. 3.3) is aligned with respect to gravity and its reflection from the grating mirror (**HRM** in Fig. 3.3) optimised so that it overlaps with the incoming beam, forming the standing light wave aligned with about 2 mrad precision. The mirror's angle θ_z about the beam axis z is then set by first introducing the mirror into the beam so that the mirror surface is cutting the transmission. The mirror is then rotated about the z-axis while monitoring the width of the transmitted stripe in real time over a 2 mm height range on the detector. If both the top

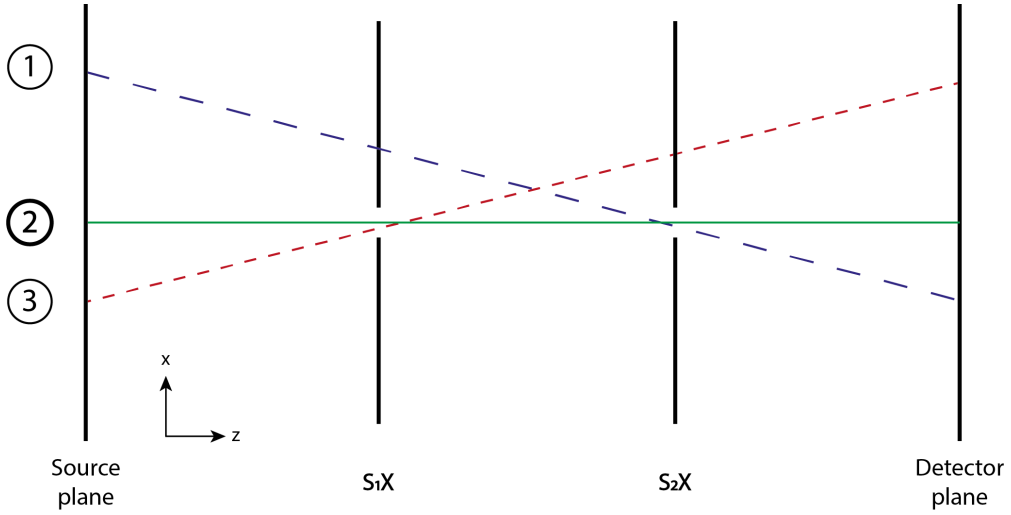

Figure 3.8: Horizontal alignment of the molecular beam, ensuring a symmetrical collimation of the molecular beam and that the transmission from the source to the detector plane is parallel to the z-axis. The position of the source laser is varied along the x-axis and the slits $\mathbf{S_1X}$ and $\mathbf{S_1X}$ alternatively narrowed until the optimal position (**2**, beam path indicated by solid green line) is reached and the stripes transmitted through both slits are centred around the same position. Positions **1** and **3** (dashed beam paths) may allow for transmission, but at an angle to the flight axis z, leading to uneven collimation when closing the second slit.

and the bottom edge of the mirror are in the yz-plane, the width of the molecular beam should remain constant over the detector height. Since the width measurements were inconclusive due to transmission artefacts, we monitored the beam edge at half the maximum intensity instead, obtaining the angular alignment better than 1 mrad, which was deemed sufficient.

The grating angle about the y-axis, θ_{grat}, is aligned in two stages. The principle is illustrated in Fig. 3.9: looking from above, the mirror should be parallel to the beam's edge, so that the transmitted stripe is as wide as possible.

For rough tuning, the mirror is rotated in approximately 0.5 mrad step and the width either read out by hand or extracted from a Gaussian fit of the transmitted stripe's trace. Since the mirror holder's range is 8 mrad, it needs to be additionally rotated by hand until the width reaches a maximum within one scan range. Once that happens, the stripe width can be plotted against the piezo's voltage and fitted linearly to obtain the approximate zero position, as shown in Fig. 3.10.

Fine tuning is done by rotating the mirror in smaller 50–100 µrad steps and looking for diffraction. If necessary, the diffraction intensity and separation can be optimised by rotating the lens **L3** in its holder and changing the grating's orientation without influencing its dimensions.

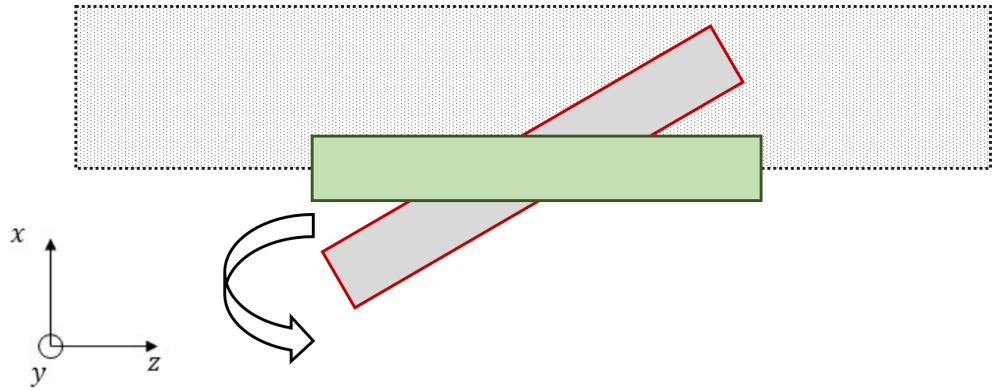

Figure 3.9: Top view of rough alignment of the grating mirror with respect to the y-axis. The mirror is rotated about the axis to maximise the width of the transmitted stripe, ensuring that the mirror's edge is parallel to the edge of the molecular beam.

3.4.3 Velocity selection and molecule-grating alignment

Desorbed molecules fly through the setup following a free-flight parabola, depending on their initial velocity. As they follow a roughly thermal distribution, the beam contains a range of de Broglie wavelengths, leading to limited spectral coherence (Eq. (3.2), $L_c = \lambda_{\mathrm{dB}}^2/\Delta\lambda_{\mathrm{dB}}$). By introducing a 25 µm tall slit $\mathbf{S_y}$ into the molecular beam, the molecular beam is split into velocity classes landing at different heights of the detector plate, as illustrated in Fig. 3.11. A smaller velocity spread leads to a reduction in $\Delta\lambda_{\mathrm{dB}}$, improving the molecules' spectral coherence.

This behaviour is described by [75]

$$v^2 = \frac{\frac{1}{2}g(LL_1 - L^2)}{y_2 - y_0 - (y_1 - y_0)\frac{L_1}{L}} \tag{3.3}$$

where L and L_1 are the distances between the source and the detector or the velocity selector slit $\mathbf{S_y}$ respectively (see Fig. 3.11). The source height from which the molecules are desorbed is denoted by y_0, the height at which molecules pass the slit y_1 and the landing height in the detector plane y_2. Since the detector size is much smaller[9] than the source-detector distance L, the forward velocity of the molecules v is assumed to be much larger than the vertical component. If only the velocity splitting relative to the slit position is of interest, Eq. (3.3) becomes

$$y_2 = y_{\mathrm{det}} = -\frac{g}{2v^2}L(L - L_1) \tag{3.4}$$

where, for simplicity, the slit height is set to $y_1 = 0$. This vertical separation can further be used to determine the forward velocity of diffracted molecules. In case of material gratings, providing clear separation of diffraction orders, Eq. (3.3) can be used to extract velocities for molecules landing on different heights at the detector screen. For Bragg diffraction measurements, the forward

[9] 2 mm compared to roughly 2 m.

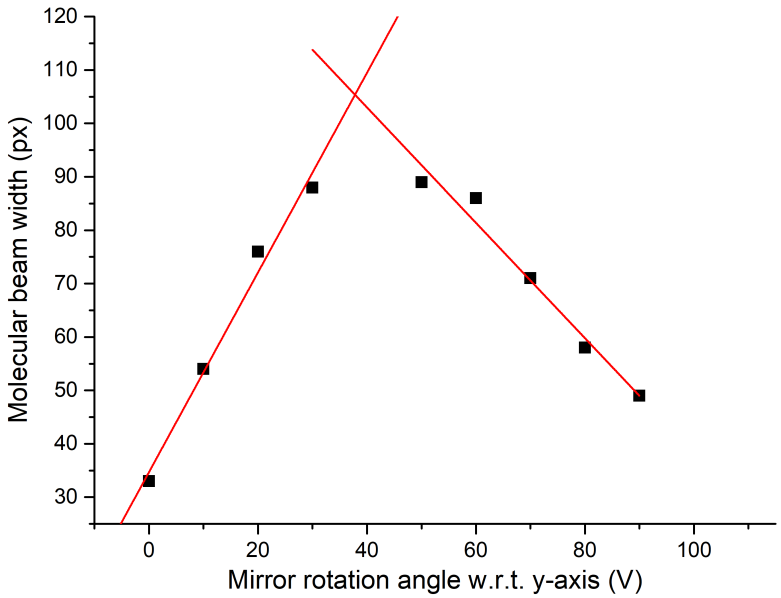

Figure 3.10: Transmitted stripe's width plotted against the piezo's voltage for rough alignment of the grating mirror with respect to the y-axis. The position at which the transmitted stripe is the widest is found at the intersection of two linear fits, here at 37.8 V, indicating the approximate zero-angle position.

velocity was estimated by comparison with three-slit grating diffraction of PcH_2 presented in [75]. To that end, the velocity distributions are measured by dividing the detector height range into thin stripes and plotting the number of registered counts in each stripe against its corresponding height. Knowing the molecular velocities in the triple slit diffraction pattern, the Bragg diffraction velocities are obtained by aligning both velocity distributions with respect to their maxima and extracting them from the known triple slit velocities and the distributions' overlap.

As previous experiments [76] have shown the need to monitor the vertical overlap of the molecular beam with the laser grating, a fibre beam profiler (see [77] and Section 5 for a detailed description) was introduced into the current version of the setup. A stripped and polished core of a multimode quartz fibre, mounted to a four-axis manipulator, is used to measure the profile of the laser grating (Fig. 3.12) and find the position of the maximal grating power. The fibre position is read out and adjusted using a HEIDENHAIN ND 218B position sensor. By depositing molecules against the fibre tip placed at the maximum of the grating, the maximum is visualised as a shadow on the detector screen where transmission is blocked by the fibre, as illustrated in Fig. 3.13. By aligning the velocity selection slit to this shadow, the fastest transmitted molecules will interact with the grating in the region where the power is the highest. Since the slit height is small compared to the peak width, all diffracted molecules are assumed to experience roughly constant grating power.

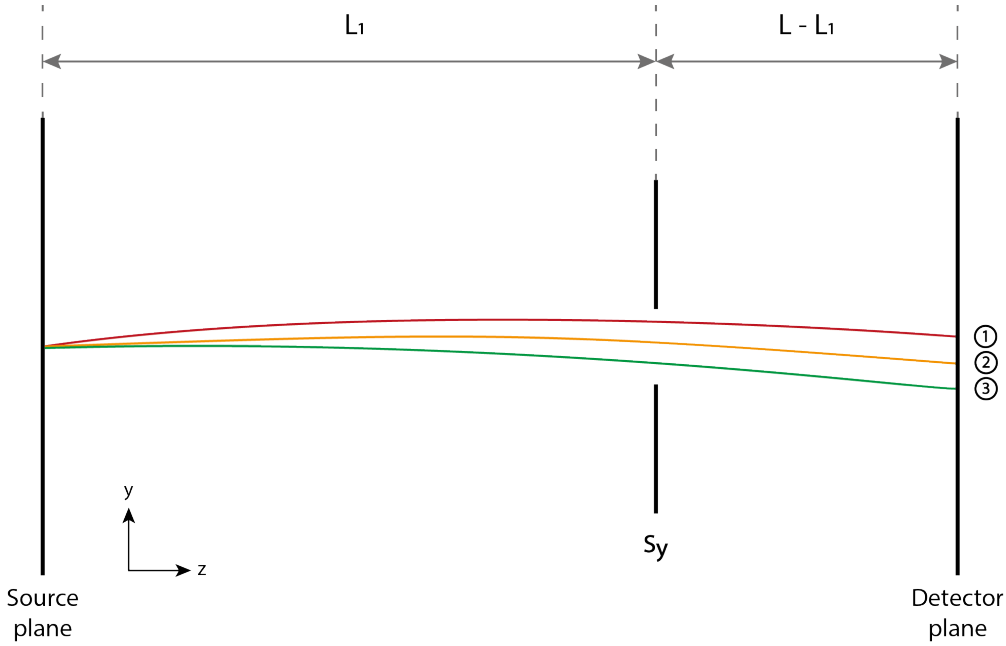

Figure 3.11: Velocity-dependent separation of molecules in the detector plane. Desorbed molecules follow a free-fall parabola and land on the detector plates at different heights, higher up for higher velocities (position **1** in the detector plane) and lower for slower molecules (positions **2, 3**). Velocity selection is done by a 25 µm tall slit $\mathbf{S_y}$.

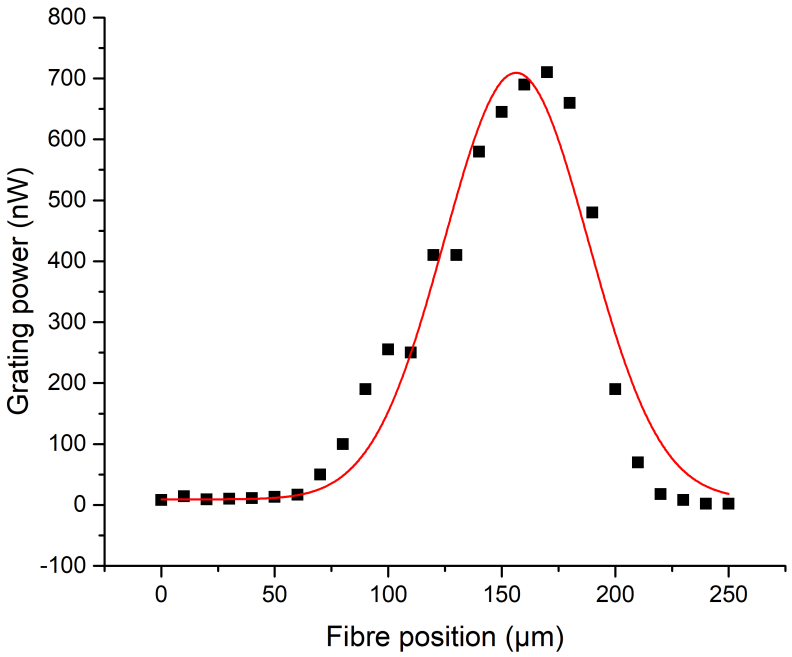

Figure 3.12: Example profile of the Bragg diffraction grating along the y-axis, as measured using the fibre beam profiler. The red line is a Gaussian fit with a $63.5(45)$ μm $1/e^2$ waist.

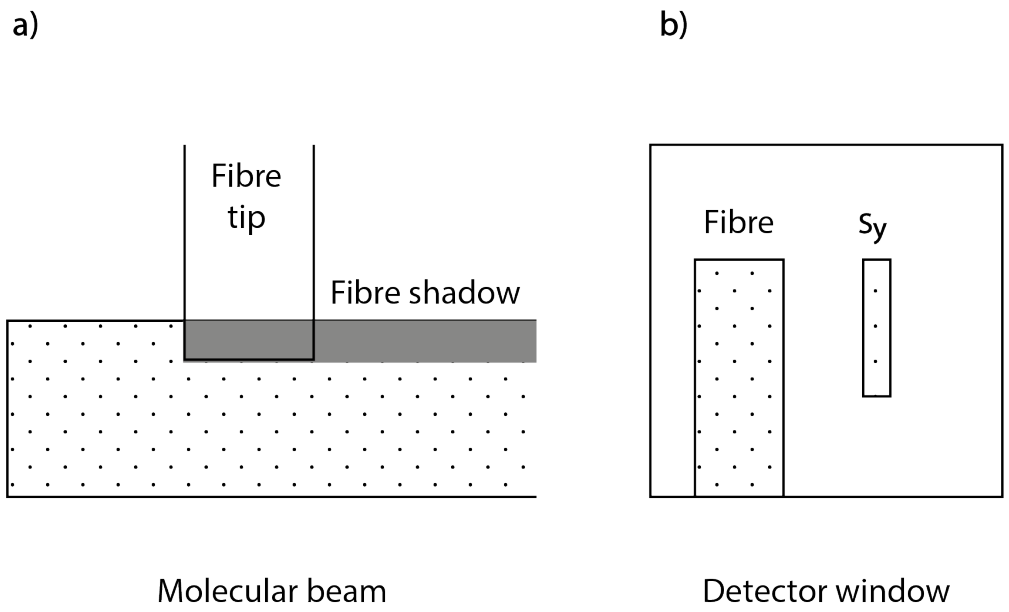

Figure 3.13: Using a fibre tip to vertically align the molecular beam and the laser grating. **a)** Vertically introducing a fibre tip into the molecular beam so that part of it is blocked introduces a shadow seen as a sharp cut-off in transmission (dotted shade) in the pattern on the detection screen **b)**. By aligning the velocity selection slit $\mathbf{S_y}$ to the fibre's shadow, transmitted molecules are directed to the maximal grating power, as measured by the fibre profiler.

4 Bragg diffraction

4.1 Overview

Bragg diffraction was first demonstrated in interference experiments reflecting x-rays from crystal planes [78]. As illustrated in Fig. 4.1, x-ray beams reflected off two parallel crystal planes can interfere if the condition

$$l\lambda = 2d\sin\vartheta \tag{4.1}$$

is satisfied. Here the integer $l \in \mathbb{N}$ denotes the order of Bragg diffraction, ϑ the incidence angle, λ the x-ray wavelength and d the separation between crystal planes. Besides its extensive use

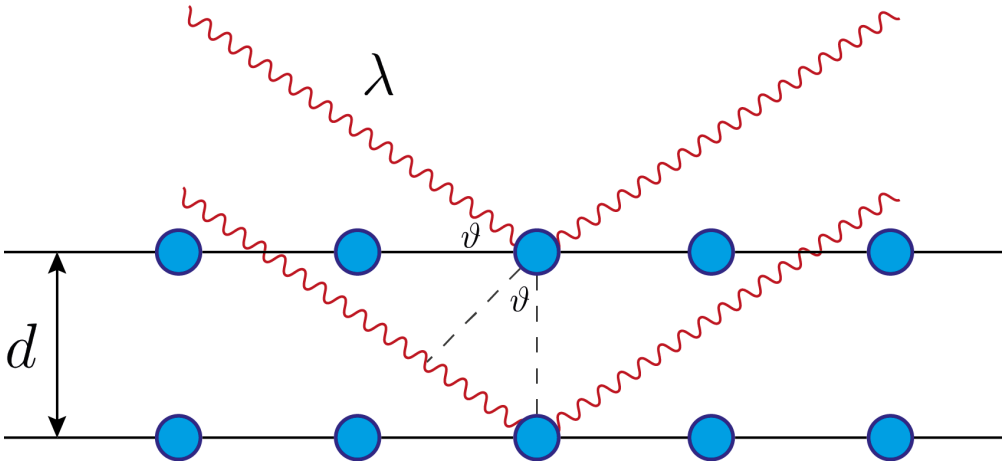

Figure 4.1: Illustration of first mention of Bragg diffraction, as diffraction of x-rays of wavelength λ on parallel crystal planes. The reflected beams interfere destructively or constructively, depending on their relative path difference.

in crystallography and x-ray spectroscopy, Bragg diffraction has found uses and applications in various areas. Examples include acousto-optic modulators used to shift laser pulses [79], optical elements such as in-fibre diffraction gratings, tunable refractive index modulators and fibre-based lasers employed as high-temperature sensors. [80–82].

Bragg diffraction is, furthermore, extensively employed in matter-wave interferometry as one of the key beamsplitting techniques. First experimental realisations were presented for neutrons diffracting on single crystals much in the similar manner to x-ray diffraction [83–85]. Already these early works discuss the so-called *Pendellösung*, a term for how the diffraction orders' populations oscillate depending on the incidence angle or the grating power. Additionally, they note the pattern's high sensitivity to parameter changes, suggesting exploring it for precision measurements.

The first neutron interferometer [5], likewise using a silicon crystal, was an important step in this direction, demonstrating interference and its dependence on phase shifts by varying neutrons' path lengths. Recombination of split beams resulting in interference further confirmed Bragg diffraction as a coherent beamsplitter for neutrons.

The first Bragg diffraction of atomic beams [35] was realised shortly after, employing a thick standing light wave as a grating. The ability to generate large coherent splitting, with over a hundred photon momenta [86] and with resulting superposition extending over half a meter [41] has made it an essential tool for atom optics [37] and interferometry experiments, including various precision measurements and fundamental tests of e.g. gravity and the equivalence principle [23, 25, 87, 88].

The remainder of this chapter introduces a theoretical description of Bragg diffraction for polarisable particles, followed by a presentation and discussion of its first experimental realisation for complex functional molecules with internal temperatures of 600 to 1000 K. Considering thr exceedingly large number of molecular internal degrees of freedom compared to atomic internal structure, the presented results show that Bragg diffraction can be extended from atoms (where the phase shift is well defined by the laser detuning) to systems with wide resonances and numerous excitations.

4.2 Theoretical description

Diffraction of matter at a light grating is described by considering interactions of polarizable (point) particles with an optical dipole potential, as introduced in Section 2.3. Depending on the details such as the interaction time, potential strength and the particles' properties, diffraction at a standing light wave can be classified into one of three following categories [89]. *Raman-Nath* diffraction, often referred to as a thin-grating approximation, takes place for short interaction times, neglecting the motion of the particle inside the grating. The resulting pattern is, to the first approximation, independent of the incidence angle, populating several diffraction orders. The exact intensity distribution depends on the power of the laser grating and can be described by superpositions of Bessel functions J_n in case of a pure phase grating [32].

For long interaction times, a distinction between the *Bragg regime* and the *channeling regime* is made based on the strength of the dipole potential. Bragg diffraction is characterised by weak potentials and, consequently, weak interactions in the grating, diffracting only into a few orders and strongly dependent on the incidence angle. The channeling regime, in contrast, is characterised by strong potentials. In the limiting case of very strong interactions, the incoming beam follows along the potential valleys, showing increasingly classical behaviour [89]. An interesting aspect of the channeling regime, however, is that the resulting diffraction pattern can show both Raman-Nath and Bragg-like features. The exact details depend on the particular combination of experimental parameters and the adiabaticity and the rate of change of the potential. As shown in [90] for atom diffraction, a fast, non-adiabatic switching on of the optical potential will lead to Raman-Nath like patterns. If, on the other hand, the potential is introduced adiabatically, population of diffraction orders will, likewise adiabatically, follow the population of energy eigenstates. If the Bragg condition (Eq. (4.1)) is fulfilled, energy conservation allows only two degenerate

eigenstates to be populated. The contributions of these two states interfere after leaving the potential, forming a two-beam diffraction pattern characteristic for Bragg diffraction.

The starting point for the Bragg diffraction experiments presented in this thesis is a molecular beam propagating with velocity $\boldsymbol{v} = (v_x, v_y, v_z)$ along the z-axis, so that $v_z \gg v_x, v_y$ and a standing light wave grating along the x-axis (see Fig. 3.1 for the coordinate system's orientation). The forward momentum of the molecules $p_z = mv_z$ and their kinetic energy $E_{\text{kin}} = mv_z^2/2$ are, respectively, significantly larger than the momentum of the grating photons $\hbar k_{\text{ph}} = 2\pi h/\lambda$ and the dipole potential's depth. Furthermore, since the forward velocity is much larger than the x- and y-component, the molecules are assumed to pass the grating without any change in height, so that the motion in both y- and z- directions remains unaffected. The problem is hence reduced to a tractable one-dimensional case where molecular interaction with the grating is considered only in the x-direction. By considering a reference frame comoving with the molecules with velocity v_x the picture is further simplified so that molecules are at rest while the grating is moving.

The Hamiltonian of the molecule-grating system is

$$\hat{H} = -\frac{\hbar^2}{2m}\frac{\partial^2}{\partial x^2} - V(t)\cos^2\left[k(x+vt)\right] \tag{4.2}$$

where the first term describes the kinetic energy of molecules with mass m and $V(t)$ is the time-dependent potential of a standing light wave whose spatial variation is described by the squared cosine term. The potential itself has the form

$$V(t) = \frac{16P\alpha'}{cw_z w_y}\exp\left(-2\frac{v_z^2 t^2}{w_z^2}\right) \tag{4.3}$$

and depends on the laser power P, the static polarizability volume $\alpha' = \alpha/4\pi\varepsilon_0$ and the $1/e^2$ grating beam radii in y- and z-directions $w_{y,z}$. The time-dependent Schrödinger equation

$$i\hbar\frac{\partial}{\partial t}\psi(t,x) = \hat{H}\psi(t,x) \tag{4.4}$$

can then be solved using the ansatz

$$\phi(t,x) = \exp\left(-\frac{i}{2\hbar}\int_{-\infty}^{t}\mathrm{d}t'\,V(t')\right)\psi(t, x+\pi/2k) \tag{4.5}$$

which can be Fourier decomposed to

$$\phi(t,x) = \sum_{j=-\infty}^{\infty} c_j(t)e^{ik_j x/n}. \tag{4.6}$$

Note that, for each term in the sum, the temporal and spatial dependence are separated into the $c_j(t)$ coefficient and the exponential term. The choice of $n \in \mathbb{N}$, an arbitrary integer determining the separation of the basis states, depends on the illumination conditions. While $n = 1$ suffices for plane wave illumination, numerical simulations, especially with finite collimation, require $n \gg 1$. Inserting this ansatz into the Schrödinger equation results in Raman-Nath equations for the time-dependent coefficients

$$i\frac{\mathrm{d}c_j(t)}{\mathrm{d}\tau} = \left(\frac{j}{n}\right)^2 c_j(t) + \frac{\gamma}{4}e^{-2r^2/\sigma^2}\left[c_{j-2n}(t)e^{4ip_{\text{tr}}} + c_{j+2n}(t)e^{-4ip_{\text{tr}}}\right] \tag{4.7}$$

characterised by dimensionless parameters

$$\gamma = \frac{V(0)}{\hbar\omega_r} \tag{4.8a}$$

$$\sigma = \frac{w_z\omega_r}{v_z} \tag{4.8b}$$

$$p_{\mathsf{tr}} = \frac{mv_x}{\hbar k} \tag{4.8c}$$

representing the grating strength, interaction time and the particle's transverse momentum, respectively. In addition, the recoil frequency ω_r is used to define the dimensionless time τ as

$$\omega_r = \frac{1}{\hbar}E_{\mathsf{kin}} = \frac{\hbar k^2}{2m} \tag{4.9a}$$

$$\tau = \omega_r t \tag{4.9b}$$

This approach, well suited for direct numerical simulations, calculates the diffraction in momentum space, with the squared coefficients $|c_j(t)|^2$ determining the populations of diffraction orders. While solving the Raman-Nath equations is in general non-trivial, closed form approximations are available in the limit of Raman-Nath diffraction, when dimensionless parameters satisfy $\sigma p_{\mathsf{tr}} \ll 1$, $\sigma\sqrt{\gamma} \ll 1$ and the weak potential limit corresponding to Bragg diffraction. In the latter case, for large transverse momentum $p_{\mathsf{tr}} > 1$, the grating strength should satisfy $\gamma \ll 8(p_{\mathsf{tr}} - 1)$ [91].

Outside of these two edge cases, solutions can be obtained numerically or by adiabatic expansion [91], starting with the Schrödinger equation and assuming a process slow enough to be adiabatic. An alternative analytical approach to the Raman-Nath equations is found in the Mathieu equations: starting with the time-independent Schrödinger equation and reintroducing the time dependence into Mathieu functions, one can obtain the complete time evolution. Similarly to the Raman-Nath equations discussed above, the Mathieu equations can be approximated for limiting cases. They are often used when the potential is non-adiabatic or suddenly switched on and off, as the number of states needed to solve Raman-Nath equations would quickly increase enough to make even numerical solving significantly harder [89].

4.3 Experimental Bragg diffraction

The experimental setup and alignment procedures have been introduced in detail in Chapter 3. This section presents the results of diffraction of ciprofloxacin and a direct comparison with a numerical simulation according to Raman-Nath equations (Eq. (4.7)), followed by discussing the influence of the incidence angle and the laser grating power on diffraction of phthalocyanine. All incidence angles are measured relative to the zero-incidence found before each run by looking for a symmetrically broadened diffraction pattern of PcH_2 and checking that the diffracted beam moves further to the side from the centred undiffracted beam (Fig. 4.2). Furthermore, for the sake of clarity, the angle is measured so that a negative incidence angle $\theta_{\text{grat}} < 0$ always diffracts the beam to the left of the incident undiffracted beam.

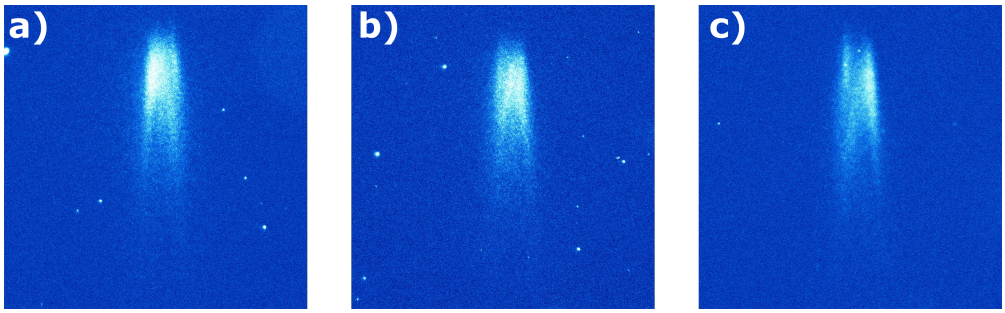

Figure 4.2: Diffraction patterns of phthalocyanine illustrating how the zero-incidence angle was determined. **a)** The incidence angle is θ_{grat} $-5(5)$ µrad, with the separated diffraction peak visible on the left. **b)** Symmetrical pattern indicating the zero-incidence angle. **c)** $5(5)$ µrad incidence, with the diffracted peak now visibly separated to the right. By convention used throughout this thesis, negative incidence angles $\theta_{\text{grat}} < 0$ lead to the beam diffracting to the left of the symmetric pattern shown in **b)**.

4.3.1 Diffraction of ciprofloxacin

Experiments with ciprofloxacin were done as single runs to be compared with numerical simulation, with an example of such comparison presented in Fig. 4.3. Due to its lower static polarizability volume, absorption cross section and fluorescence yield compared to phthalocyanine, ciprofloxacin requires longer accumulation times[10] to obtain sufficiently intensive diffraction patterns, which is why the patterns were taken as single shots instead of scan series performed with PcH_2 shown later in this chapter. The diffraction pattern was taken with grating power of 14.6 W, waists $w_z = 7.04(5)$ mm and $w_y = 55(5)$ µm. Molecular beam collimated to 14 µm was hitting the grating under a $-43(5)$ µm incidence angle. A relatively sudden onset of diffraction starts for molecules moving at about 300 m/s, populating Bragg orders from 4th to 6th. The sixth order is noticeably dominant, leading to a slight bend and broadening of the diffracted (left) peak due to non-resonant contributions of different velocities. Due to the grating's limited power

[10] Over 30 hours.

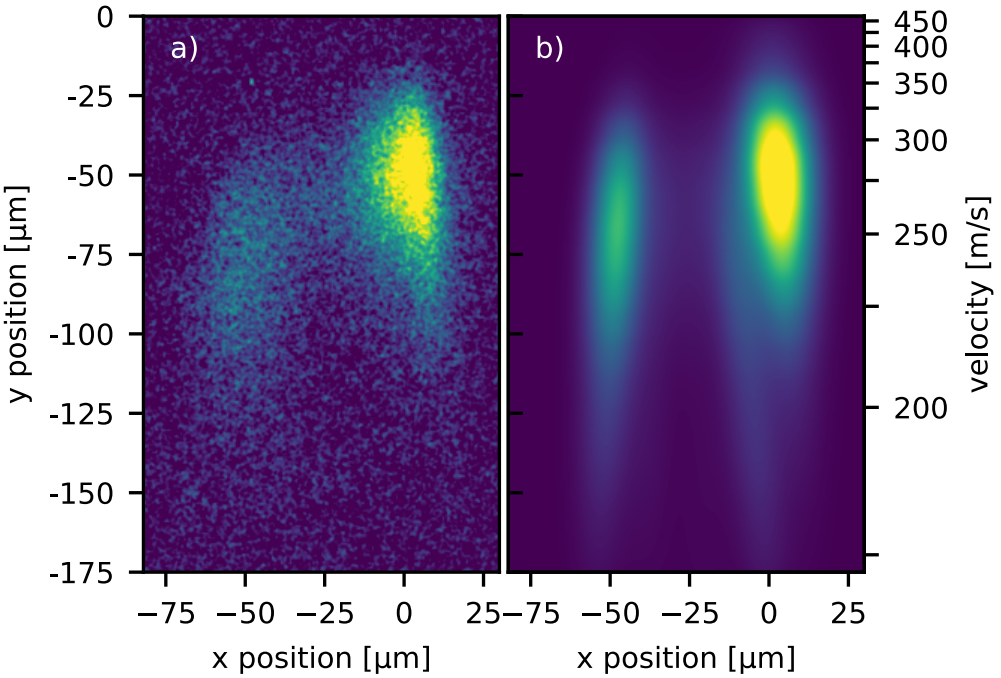

Figure 4.3: Comparison of a measured **a)** and simulated **b)** diffraction pattern of ciprofloxacin at $\theta_{\text{grat}} = -43(5)\,\mu\text{rad}$ incidence angle. The simulation is qualitatively reproduced by measured data, but shows that the Bragg condition in the measurement was somewhat relaxed due to a comparatively short interaction time [65].

and thickness in flight direction, the interaction time is long enough only for molecules slower than 300 m/s, explaining the lack of diffraction for faster molecules predicted by the simulation. The Bragg condition is hence somewhat relaxed, explaining the losses to neighbouring diffraction orders instead of the predicted diffraction-free region. By comparing the peak amplitudes and separations at different velocities, the grating is shown to act as an equal amplitude beamsplitter at 210 m/s, realising a momentum transfer of $10\,\hbar k_{\text{ph}}$ grating photon momenta.

4.3.2 Diffraction of phthalocyanine

The angular dependence of Bragg diffraction was further tested with PcH_2 by performing a series of scans, looking at how the interference pattern changes when varying the molecular beam's incidence angle and the grating power. Its larger static polarizability volume and more intense fluorescence made it a better candidate for scan-based measurement, allowing for completing the scan series in one go and ensuring that the experimental conditions stay constant. After finding the zero incidence angle, the scan was started at $\theta_{\text{grat}} = -69(5)\,\mu\text{rad}$, the largest angle for which diffraction was observed at the scan's grating power of $14.6(2)\,\text{W}$. The incidence angle was then increased in roughly 11 µrad steps and the corresponding diffraction patterns and intensity profiles recorded, as shown in Fig. 4.4. The laser grating height was $65(5)\,\mu\text{m}$ and the molecular beam collimated to 14.8 µm. The diffraction patterns are qualitatively similar to those obtained with ciprofloxacin, globally showing a single diffraction order moving from far left, over

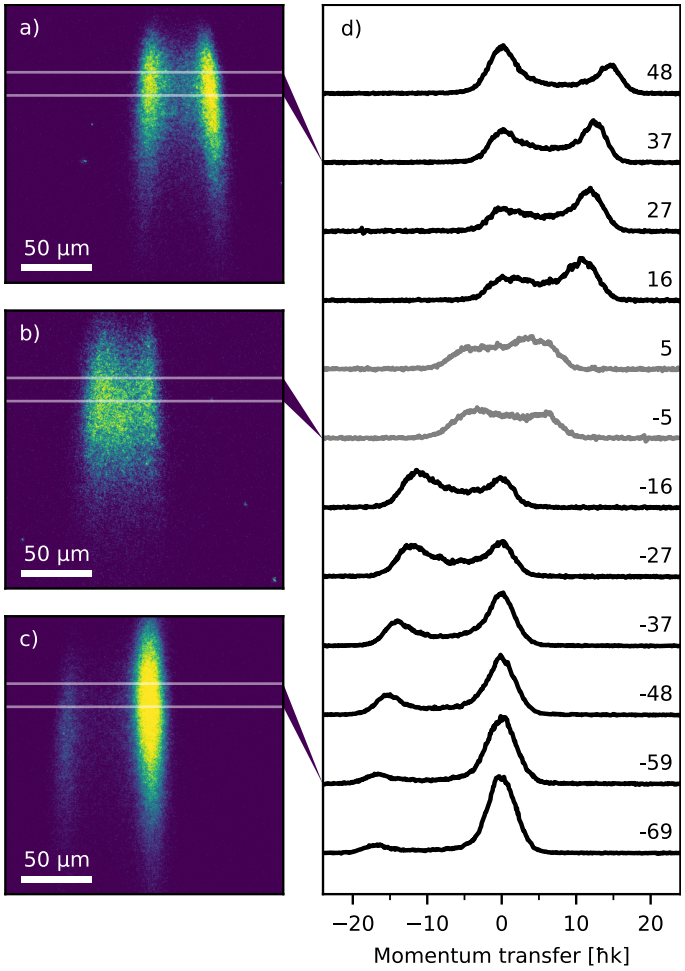

Figure 4.4: Angular scan showing Bragg diffraction of PcH_2 [65]. Panels **a)** - **c)** show diffraction images taken for incidence angles of -69, -5 and 5 µrad respectively. Integrated intensity profiles, taken for the velocity range 234 to 255 m/s as indicated by horizontal cut-outs in diffraction images, are displayed in panel **d)** and show both the characteristic single pronounced peak and the expected symmetric behaviour for $\theta_{\text{grat}} = \pm 5$ µrad, i.e. around the zero incidence angle.

the middle and to the far right with increasing incidence angle. Crossing of the zero-incidence angle is indicated by the symmetry of intensity profiles at $\theta_{\text{grat}} = \pm 5$ µrad. Furthermore, the presence of a single pronounced diffracted peak for incidence angles further away from zero again implies Bragg or Bragg-like diffraction as the primary regime. This assumption is strengthened when considering the full velocity-dependent intensity profile at 5 µrad incidence angle as shown in Fig. 4.5. Populations of the diffracted and undiffracted beam demonstrate the characteristic *Pendellösung* and oscillate with changing molecular velocity, with the diffracted (right) beam's population increasing as the undiffracted beam's population drops and vice versa.

An additional test was performed to investigate the influence of grating laser power on the diffraction pattern. The incidence angle was set to $\theta_{\text{grat}} = -30(5)$ µrad, a value that had shown large, clean separation during the angular scan. Diffraction patterns were then recorded with

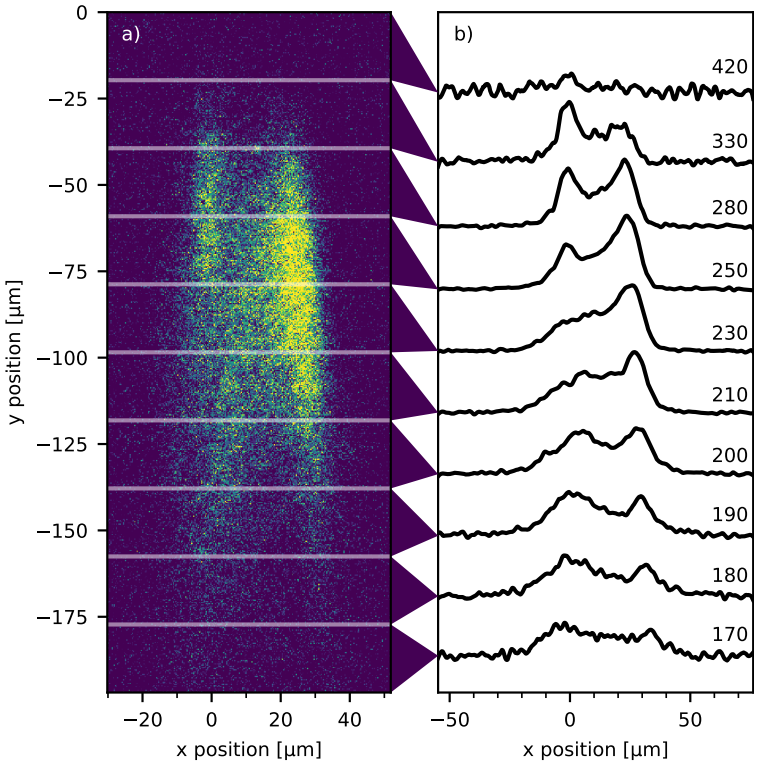

Figure 4.5: Diffraction of PcH_2 as measured for the $\theta_{\text{grat}} = 5(5)\,\mu\text{rad}$ incidence angle [65]. Panel **a)** shows the false colour diffraction image, sliced into 20 µm tall stripes whose intensity profiles are extracted and displayed in panel **b)**. Populations of diffraction orders oscillate depending on the height, and consequently, molecular velocity (indicated for each trace in m/s), showing *Pendellösung* behaviour characteristic of Bragg diffraction.

the molecular beam collimated to 12.5 µm and a $w_y = 54(2)\,\mu\text{m}$ tall laser grating whose power was varied between 12.3 W and 1 W. According to theoretical predictions, changing the potential depth should result in the diffracted beam should remain at a constant angle, with the populations of the diffracted and the undiffracted beam showing *Pendellösung* oscillations. The scan, shown in 4.6, does show the oscillating populations, but also a discrepancy where the diffracted peak is moving further away with increasing power by about 20 µrad over the course of the scan. Since the molecular source and collimation were kept constant during the scan, showing no signs suggesting instabilities, the grating angle was likely changing due to residual thermal effects of changing laser power and resulting heating of the mirror holder.

Deviations from ideal Bragg diffraction, such as losses to intermediate diffraction orders, are attributed to the intermediate diffraction regime with contributions from Raman-Nath diffraction and in-grating photon absorption as discussed in Section 3.3.1. For 12–15 W, the highest powers in these experiments, each molecule absorbs, on average, one photon upon passing through the grating which contributes to line broadening. The number of absorbed photons was estimated by collimating the transverse molecular velocity spread to roughly the grating photon's recoil

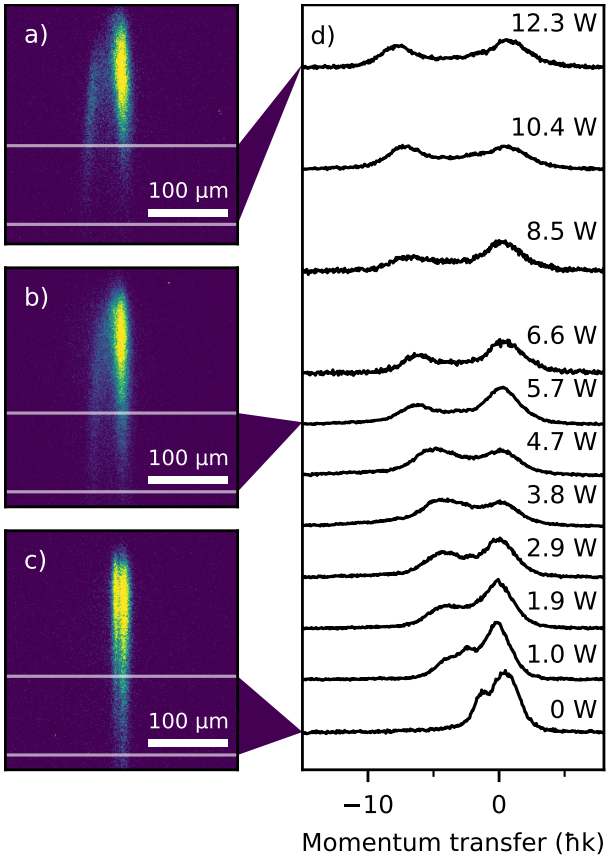

Figure 4.6: Dependence of PcH_2 diffraction pattern on laser powers ranging from 12.3 W to 1 W [65]. Diffraction images in panels **a)** and **b)** were taken at 12.3 W and 5.7 W. The double peak in **c)**, taken with the laser switched off, is an artefact of the collimation slit. Intensity profiles in panel **d)** show oscillations in populations of diffracted (left) and undiffracted beam and a power-dependent increase in diffracted beam's angular separation.

velocity and comparing the $1/e^2$ radius of the transmitted beam with[11] and without the laser grating. The broadening is illustrated in Fig. 4.7 for a 140 m/s PcH_2 beam collimated to 4 µm and a 30 W laser grating with $w_y = 44(1)$ µm. Lineshape broadening when the grating laser is introduced and the spacing of the resolved substructure are consistent with 532 nm photon recoil, implying the absorption of, on average, 2.5 photons at this intensity. The symmetric resolved substructure implies that photon reemission is not the dominant deexcitation mechanism - the energy molecules gain through absorption is rather redistributed to internal degrees of freedom in a radiationless relaxation process. Nevertheless, the angular scan measurement demonstrates a maximal momentum transfer of $18\,\hbar k_{\mathrm{ph}}$ with 10% efficiency and a $14\,\hbar k_{\mathrm{ph}}$ equal-amplitude beamsplitter, the largest momentum splitting for molecules demonstrated to date using optical gratings. While the explicit coherence of the diffracted beams has not been tested yet, it is assumed as a consequence of the quantum treatment applied throughout. To this end, decoherence via collisions with residual gas molecules was avoided by performing all measurements at

[11] At an angle where no diffraction is expected.

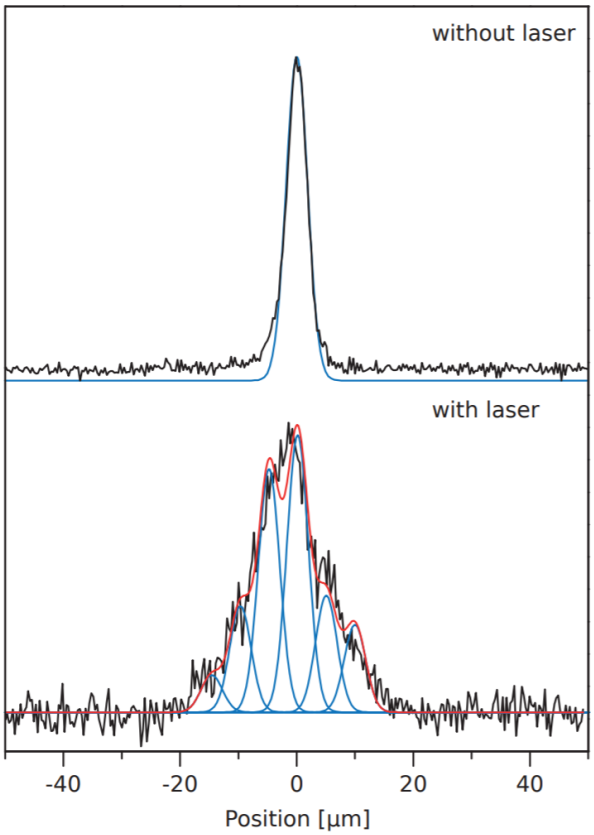

Figure 4.7: Broadening of the phthalocyanine beam due to absorption of grating photons [65]. A 140 m/s beam collimated to 4 µm absorbs, on average, 2.5 photons when passing through a 44(1) µm tall, 30 W laser grating. For 12–15 W used in the experiment, the mean number of absorbed photons is approximately one.

pressures below 10^{-7} mbar. Furthermore, fragmentation during laser desorption or in free-flight and possible reemission of photons absorbed in the grating were excluded by spectroscopic studies and resolving substructures of the transmitted peaks as detailed in Chapter 3. Drawing from these precautions removing plausible decoherence channels and results of previous successful interference experiments in the same setup, it stands to reason to assume coherence in the present case as well.

5 Fibre beam profiler

The fibre beam profiler was initially developed as a tool for aligning the molecular beam and laser grating to each other in Bragg diffraction experiments, as described in Chapter 4. This chapter shows its capabilities as a stand-alone beam profiling device [77], showcasing the compatibility with high-vacuum conditions (below 1×10^{-7} mbar) and a reliable output for laser powers ranging from 100 mW to 14 W, sustaining intensities over 2 MW/cm^2.

Most commercially available solutions for laser beam profiling rely either on cameras or moving mechanical elements. Camera-based profilers usually use CCD or CMOS chips, work best in the near-IR and visible wavelength range and often have a large active area, allowing accurate profiling of large or higher order, non-Gaussian beams. Their performance, both in terms of sensitivity and resolution, is characterised through the chip type and material. For instance, silicon-based chips work best for wavelengths up to 1100 nm, resolving beams of several tens of micrometers in size. Longer wavelengths can require the use of indium galium arsenide (InGaAs) chips or thermal infrared imaging. Care has to be taken to avoid irreversible chip damage through laser radiation, both in the UV region due to low absorption of silicon and due to high laser intensities, as CCD and CMOS chips exhibit damage already starting at 10 kW/cm^2 continuous-wave (cw) intensity [92].

Mechanical profilers rely on moving a thin element, such as a knife edge, slit or pinhole, through the beam and recording the transmitted power. The beam profile is then reconstructed electronically. Because of the reconstruction process involving summation along the scanning axis, these profilers are betters suited for nearly Gaussian beams, to avoid smoothing out higher modes. Compared to camera-based profilers, they operate in a larger wavelength range and are limited only by their mechanical element. Typically, they can sustain higher laser intensities and deliver better spatial resolution, which is limited only by the element's thickness, profiling beams down to a couple of micrometers in size.

While both profiler types work exceedingly well and have found many applications, they can be hard to implement in small spaces, such as inside the interferometer chamber in our diffraction experiments. The solution presented here uses a stripped multimode quartz fibre whose tip is inserted into the beam. Depending on the local intensity, light is scattered into the fibre on the tip surface and guided to a power meter. An intensity profile is then obtained by scanning the fibre tip across the beam, in our case using a linear micrometer stage. We combine the advantages of both solutions, avoiding possible summation issues for non-Gaussian beams due to direct local probing and a considerably higher damage threshold than camera-based solutions.

5.1 Gaussian beams

This approximation assumes uniform scattering of laser light over the entire projected core diameter, therefore providing an upper limit for the area actively collecting light. The effective area becomes lower e.g. in presence of active scattering centres on the surface, or if the light scatters only from a part of the fibre tip.

The measurements and analysis presented here focus mainly on Gaussian and near-Gaussian beam profiles, but the technique is applicable to arbitrarily shaped beams. Starting with the wave equation for propagation of the electric field $E(x, y, z)$ in vacuum

$$\Delta E(x, y, z) = \frac{1}{c^2} \frac{\partial^2 E}{\partial t^2} \tag{5.1}$$

making use of the paraxial approximation for a field propagating in z-direction

$$\frac{\partial^2 E}{\partial z^2} \ll \frac{\partial^2 E}{\partial x^2}, \frac{\partial^2 E}{\partial y^2} \tag{5.2}$$

and assuming that the corresponding wave envelope varies slowly as

$$\frac{\partial^2 E}{\partial z^2} \ll k \frac{\partial E}{\partial z} \tag{5.3}$$

an ansatz for the electric field can be written as

$$E(x, y, z) = u(x, y, z) \cdot e^{i(\vec{k} \cdot \vec{r} - \omega t)} \approx u(x, y, z) \cdot e^{ikz}. \tag{5.4}$$

Rewriting the wave equation (Eq. (5.1)) under these assumptions yields the paraxial Helmholtz wave equation

$$\frac{\partial^2 E}{\partial x^2} + \frac{\partial^2 E}{\partial y^2} = 2ik \frac{\partial E}{\partial z}. \tag{5.5}$$

Solutions of this equation are given by transverse electromagnetic modes, TEM_{mn}. The fundamental mode TEM_{00} is the lowest order, cylindrically symmetric solution, given by

$$E(x, y, z) = \frac{1}{\sqrt{1 + (z/z_R)^2}} \exp\left\{ -i \left[kz - \arctan\left(\frac{z}{z_R} \right) \right] - i \frac{kr^2}{2q} \right\} \tag{5.6}$$

and often called simply Gaussian beams. Here z is the coordinate along rhich the beam propagates, $k = |\vec{k}|$ is the absolute value of the wave vector and $r = \sqrt{x^2 + y^2}$ is the radial coordinate transverse to the beam propagation direction. The Rayleigh length

$$z_R = \frac{\pi w_0^2}{\lambda} \tag{5.7}$$

is inversely proportional to the laser wavelength λ and is the distance from the focal point in which the minimal beam waist w_0 increases by a factor of $\sqrt{2}$, to $w = \sqrt{2} w_0$. In general, the beam waist evolves hyperbolically with z as

$$w(z) = w_0 \sqrt{1 + \left(\frac{\lambda z}{\pi w_0^2} \right)^2} = w_0 \sqrt{1 + \left(\frac{z}{z_R} \right)^2}. \tag{5.8}$$

The complex beam parameter q gives the relationship between the beam waist, wavelength and the wave front curvature R_{wave} as

$$\begin{aligned} \frac{1}{q} &= \frac{1}{R_{\text{wave}}} - i\frac{\lambda}{\pi w^2(z)} \\ R_{\text{wave}}(z) &= z + \frac{z_R^2}{z}. \end{aligned} \tag{5.9}$$

These parameters are illustrated in Fig. 5.1, showing a transverse cross section of a Gaussian beam. Additionally, the figure shows the confocal parameter $b = 2z_R$, describing the focus' depth and the beam's diffraction-limited divergence angle

$$\Theta = \frac{\lambda}{\pi w_0}. \tag{5.10}$$

The intensity profile of a Gaussian beam is a typical bell-shaped curve (Fig. 5.2), directly

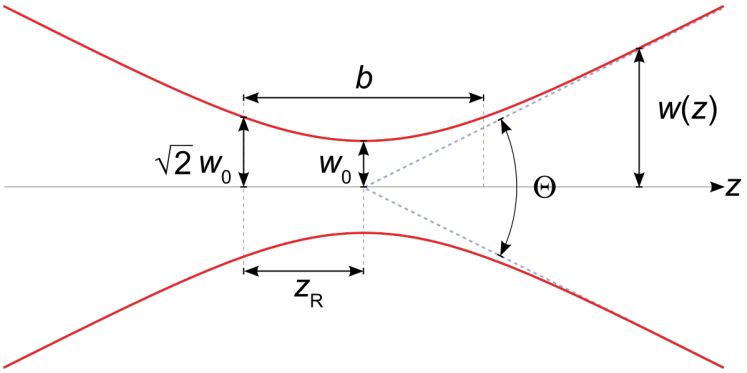

Figure 5.1: Cross section of a Gaussian beam along the propagation direction [93]. Depicted parameters are the Rayleigh length z_R, confocal parameter $b = 2z_R$, beam waist $w(z)$ and its minimum w_0, as well as the divergence angle Θ.

proportional to laser power P and given by

$$\begin{aligned} I(x, y, z) &= I_0(z) \cdot \exp\left(-\frac{2r^2}{w^2(z)}\right) \\ I_0(z) &= \frac{2P}{\pi\omega^2(z)}. \end{aligned} \tag{5.11}$$

The width of such beam profiles can be characterised in several ways, for instance using the full width at half maximum (FWHM), $1/e$ or $1/e^2$ beam radius. The analysis presented here uses the $1/e^2$ radius as illustrated in Fig. 5.2. This is the distance from the beam centre at which the intensity drops by a factor of $1/e^2$, or to roughly 13.5% of the maximum value. All provided waist values w are to be understood as $w \equiv w_{1/e^2}$.

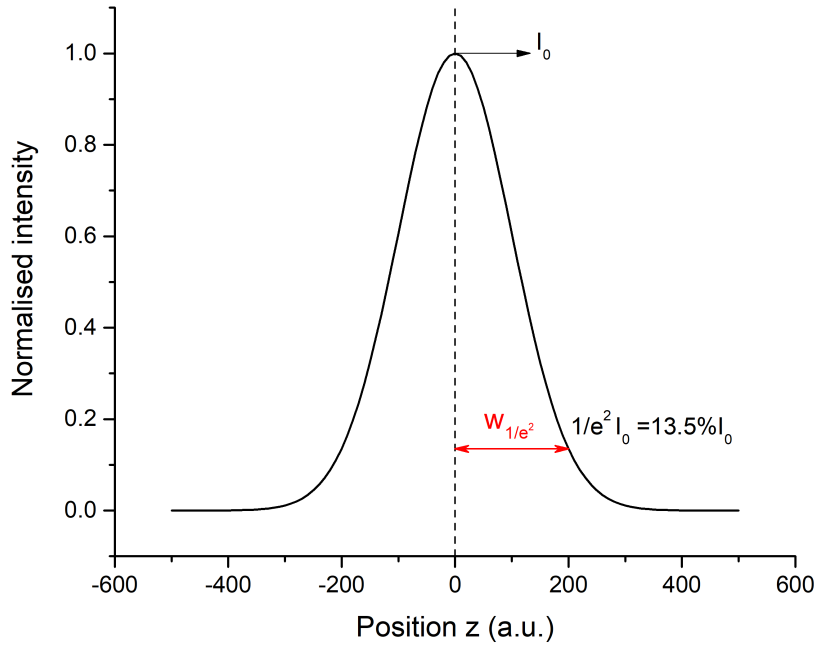

Figure 5.2: A normalised intensity profile of a Gaussian beam. The red-marked waist w_{1/e^2} is taken as beam radius and denotes the distance from beam centre in which the intensity drops to 13.5% of the maximum value.

5.2 Setup and experiments

The basic measurement principle, already introduced in the beginning of this chapter, is shown in Fig. 5.3: a stripped fibre tip is moved into the laser beam propagating in z-direction, then scanned in either x- or y-direction with micrometer precision using a linear stage. The fibre guides the light scattered into the tip to a power meter and the beam profile is obtained by plotting the recorded power against the position of the fibre tip.

All measurements were done using a single frequency 532 nm Coherent Verdi V-18 laser. The setup for measurements done in air, schematically shown in Fig. 5.4, is virtually identical to preparation of the laser grating for Bragg diffraction, except for the quarter-wave plate taken out as there is no direct reflection back into the laser. The beam is expanded to $w_x = w_y = 7.04(5)$ mm using a 1:6.25 telescope built out of lenses **L1**, **L2** (focal lengths $f_1 = 40$ mm and $f_2 = 250$ mm, respectively), then focused vertically along the x-axis using the cylindrical lens **L3** with $f_3 = 250$ mm focal length, placed on a micrometer linear stage. The fibre guides the scattered light to a Newport 818-UV detector head connected to the Newport 1830-C power meter **PM**. The half-wave plate $\boldsymbol{\lambda/2}$ is used to adjust the laser power.

The fibres used for measurements in air were a 10 µm core (Thorlabs M65L01, wavelength ranges 400–550 nm and 700–1000 nm), 50 µm core (Thorlabs M16L01, 400–2400 nm) and a

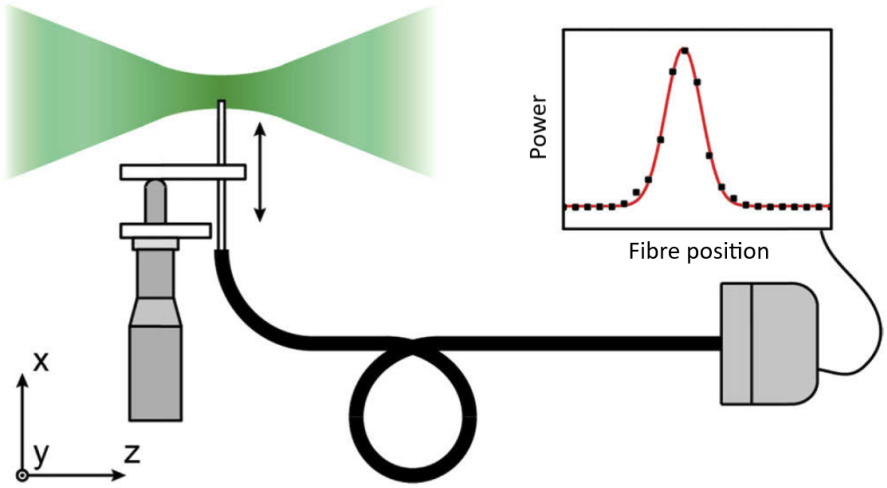

Figure 5.3: Basic principle of operation of the fibre beam profiler [77]. A stripped fibre tip is moved into the beam, then scanned with micrometer precision while the scattered light is directed to a power meter and plotted against the position of the tip to obtain an intensity profile.

1000 µm core (THORLABS M71L02, 400–2200 nm). Vacuum measurements were done using a 50 µm core fibre. All fibres were stripped at the tip, removing the PVC jacket tubing and inner coating, so that only the polymer-based cladding and the quartz core were left. To prepare flat tips, the 10 µm core fibre was simply cut with a pair of pincers, while the 50 µm core fibres were first cut using a fibre cleaver, then roughened using a 30 µm grit size polishing sheet. The roughening step was needed to ensure a sufficient number of scattering centres, as the pristinely cut fibre scattered no light into the detector. Figure 5.5 shows microscope images of two tips used for measurements in air. To see how the tip-air coupling interface looks like, light from a LUMENCOR illuminator was coupled into the other end of the fibre. Visible as bright spots at the tip in Fig. 5.5, light scatters out of the fibres at right angles and, as expected, only from the core area.

Reference data were obtained using a knife-edge based beam profiler, COHERENT BEAM MASTER. The laser power was reduced to 7 mW and the profiler placed into the focus after the lens **L3** as indicated by maximal measured power. The lens was then moved in 0.5 mm steps and a beam profile recorded at each position.

For measurements in air, the fibres were fixed to a linear micrometer stage pointing in either x- or y-direction (Fig. 5.3). For each position of the focusing lens **L3**, moved in 0.5 mm steps, the beam profile was measured by moving the fibre in 10 µm steps and recording the corresponding transmitted power. To ensure stability, this power was also monitored over several hours. For vacuum tests, done at $p < 1 \times 10^{-7}$ mbar, the beam was initially focused with a cylinder 250 mm focal length lens as **L3** and measured in 10 µm steps as measured with a HEIDENHAIN ND 218 B sensor, for different lens positions and orientations and over the course of several months and Bragg diffraction experiments. High-intensity tests and compatibility with different powers were performed focusing the beam with a spherical, again $f = 250$ mm, lens as **L3** for laser powers

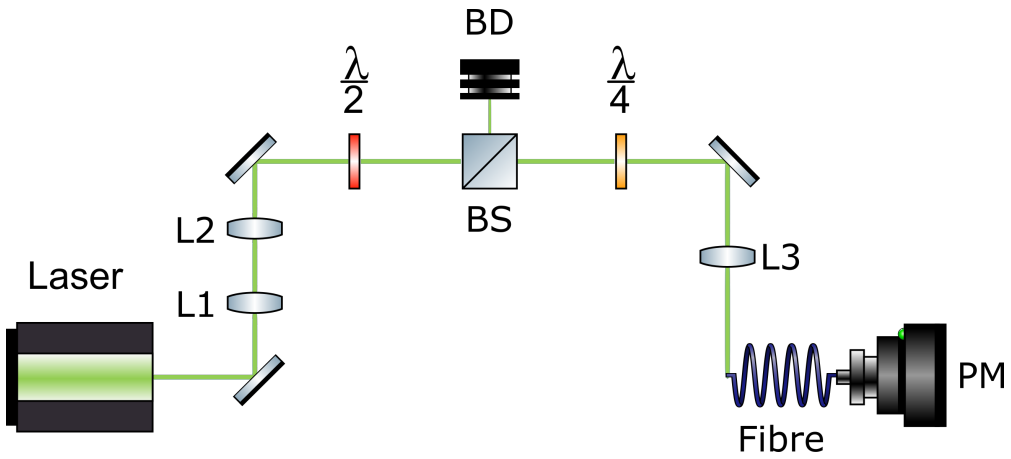

Figure 5.4: Diagram [66] of the fibre profiler setup for measurements in air. The laser beam is expanded using a telescope consisting out of lenses **L1** and **L2** ($f_1 = 40\,\text{mm}, f_2 = 250\,\text{mm}$), directed to a half-wave plate $\boldsymbol{\lambda/2}$, then vertically focused along the x axis using the cylindrical lens **L3** with $f_3 = 250\,\text{mm}$. Light is then guided by the fibre to a power meter **PM**. Double-headed arrows indicate that the corresponding component is movable with micrometer precision.

ranging from 130 mW to 14.6 W and checking for damages to the fibre tip.

All resulting traces, measured both using the fibres and the moving edge profiler, were fitted to a standard Gaussian curve

$$y(x) = y_0 + \frac{A}{w\sqrt{\pi/2}} \exp\left(-2 \cdot \left(\frac{x - x_c}{w}\right)^2\right) \tag{5.12}$$

to extract the waist w. The minimal beam waists w_0 were then determined by fitting the measured waists w against lens positions using the slightly modified Eq. (5.8)

$$w(x) = w_0 \left[1 + \left(\frac{x - x_c}{z}\right)^2\right]^{1/2}. \tag{5.13}$$

Here the Rayleigh length z_R is encoded in the free parameter z, while x_c gives the lens position corresponding to the minimal waist w_0.

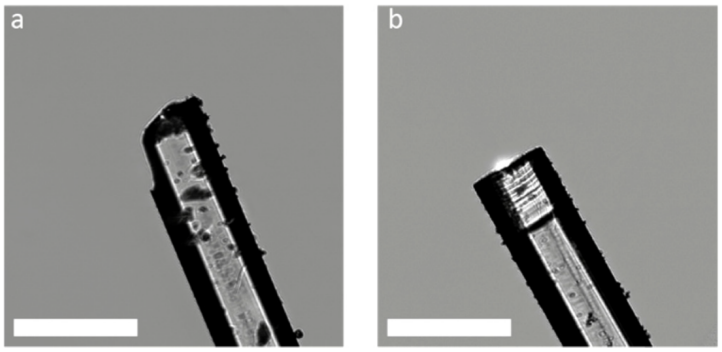

Figure 5.5: Microscope images [77] of illuminated typical fibre tips used in the experiment, with **a)** 10 µm and **b)** 50 µm core diameter. Bright spots at the tips show that light used for illumination scatters out of the fibre at right angles. The scale bar corresponds to 200 µm.

5.3 Results and discussion

5.3.1 Theoretical model and evaluation

A simple model for estimating the measured beam profile can be obtained by convoluting the laser intensity with a position-dependent kernel $K(x)$ describing the fibre

$$K(x) = \mathrm{Re}\sqrt{\left(\frac{r}{2}\right)^2 - x^2}. \tag{5.14}$$

Here r is the projection of the diameter of the fibre core diameter R onto the axis in which the beam profile is measured, and is hence bounded by the core size, too. For a beam propagating in the z-direction and profiled in x-, with the fibre tip making an angle θ with the z-axis (Fig. 5.6), this projection can be estimated as

$$r = R\sin\theta. \tag{5.15}$$

The idea behind the convolution kernel as defined in Eq. (5.14) is shown in Fig. 5.7. For a fibre surface moved perpendicularly into the beam, the surface kernel is obtained by slicing the surface into chords of length

$$s = 2\sqrt{\left(\frac{R}{2}\right)^2 - \left(\frac{R}{2} - h\right)^2} \tag{5.16}$$

and plotting $s/2$ against height h ranging from $-R/2$ to $R/2$, so that the obtained kernel is semi-circular. In general, the kernel is elliptical and dependent on the incidence angle between the core surface and the laser beam, requiring the projection onto the measurement axis (Eq. (5.15)) to be used instead of the radius $R/2$. When the relative angle θ is increased, the kernel's ellipse becomes narrower while staying at the same height, until it eventually reaches a delta function-like form for $\theta = 90°$.

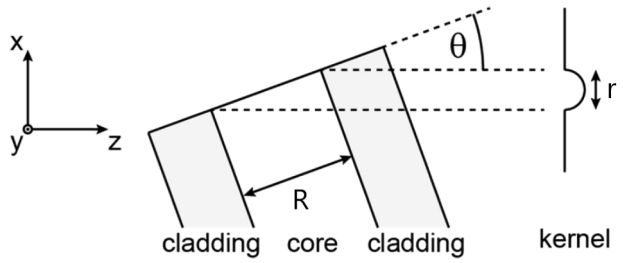

Figure 5.6: The effective diameter of the fibre core can be estimated as a projection of the core on the axis in which the beam profile is measured. Here the beam propagates along the z-axis, while x is the measurement direction [77].

The validity of the model and its sensitivity to alignment can be tested by comparing its predictions to simulated Gaussian beams of a given width. While the convolution implies that the measured beam will always be wider than the simulated Gaussian, a 50 µm core fibre under a $\theta = 10°$ angle will overestimate the waist of a nominally $w = 10$ µm wide beam only by about 1 µm (illustrated in Fig. 5.8), or about 0.6 µm for a $w = 15$ µm beam. For larger beams, the relative error drops even further. An even better accuracy can be obtained by precisely aligning the fibre to reduce the tilt angle θ, but even moderately good alignment and core sizes can achieve high-resolution beam profiling where the beam is several times narrower than the core. This is further confirmed by comparing single beam profiles, as measured with the moving edge profiler, 10 µm and 50 µm core fibres and shown in Fig. 5.9. The $33.9(1)$ µm reference width is reproduced well both by the 10 µm core with $32.6(1.2)$ µm and 50 µm core with $34.6(1.2)$ µm, deviating by 2% and 3.8% respectively. Despite being only about 10 µm wide, the small shoulder to the right of the beam centre is measured by both fibres, again demonstrating high-resolution capabilities even of the wider 50 µm core and for the 10 µm step size.

5.3.2 Profiling in air

Profiles and minimal waists in air were measured transversely and longitudinally with respect to the beam propagation direction z, with the coordinate system as shown in Fig. 5.3. For transverse measurements the fibre tip was in the xz-plane and moved along the x-axis. To make the comparison easier, the extracted waists are centred around zero with respect to the focal point, i.e. the minimal waist's position, as shown in Fig. 5.10. The error bars represent fit uncertainties as taken from each profile's respective Gaussian fits. Globally, both fibres produce good agreement with the $w_0 = 5.8(4)$ µm reference: $6.9(5)$ µm for one of the 50 µm cores and $6.6(3)$ µm for the 10 µm core. The other 50 µm core shows a large, albeit consistent overestimation, measuring $w_0 = 32.1(1.4)$ µm. Since both tips were cut and prepared in the same way, the discrepancy is likely due to some combination of the overestimating tip making a larger angle with the beam axis and microscopic differences in the tip surfaces due to the roughening by polishing sheet being done by hand only. Even so, the measured width is below the maximum broadening of 40 µm predicted by the model, calculated for the edge case where $\theta = 90°$.

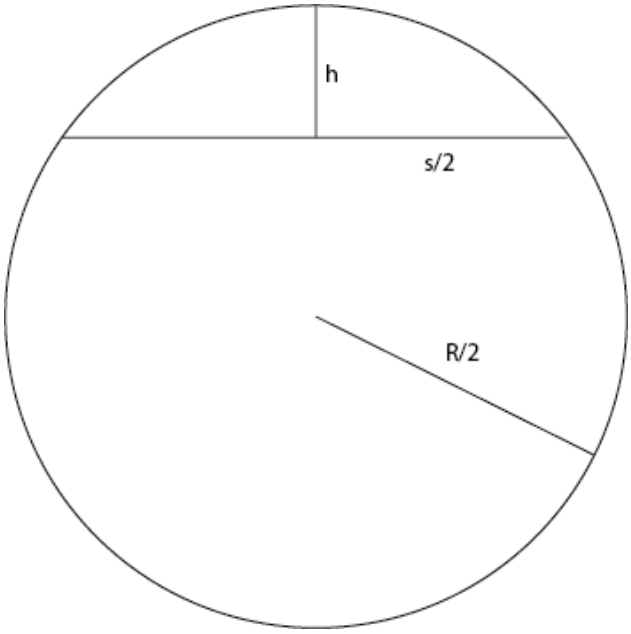

Figure 5.7: For a circular fibre core moved perpendicularly into the laser beam, the coupling element's semicircular kernel is obtained by plotting half the chord length $s/2$ against its corresponding height h between $-R/2$ and $R/2$. In a more general case, the obtained kernel is elliptical and dependent on the incidence angle between the beam and the coupling surface.

To test the fibre's capabilities as a two-dimensional beam profiler, a series of longitudinal scans was performed and shows very similar results. For these measurements, the fibres were introduced into the beam from above, so that the tip was in the yz-plane and scanned along the x-axis. The extracted widths are centred as in the transverse case and shown in Fig. 5.11. The minimal reference width is $w_0 = 5.8(4)$ µm, same as in the transverse case. The overestimate by the 50 µm and 10 µm cores is now somewhat larger, resulting in $7.9(1.2)$ µm and $9.5(6)$ µm respectively. The second 50 µm core stands out again, but broadens the signal significantly less, to the effect of $16.3(3)$ µm. Combined with the now larger discrepancy for the 10 µm core, this suggests that the tip's angular alignment has a greater influence on measured broadening than the already consistent tip preparation method, reducing the possible impact of microscopic surface variations. Furthermore, in both longitudinal and transverse measurement, the values obtained from both differently sized cores are in good agreement, with the larger core inducing only marginally larger broadening as long as the cores are somewhat comparable in size to expected beam widths. Additional tests performed with a 1000 µm core fibre under same conditions are shown in Fig. 5.12 and display seemingly arbitrary non-Gaussian profiles which do not change over a 2 mm distance, suggesting oversaturation due to the core being large in comparison to the beam width.

The fibres have shown no signs of laser-induced damage to tips for measurements done over several weeks. To test for compatibility with high powers, the beam was focused on the 10 µm tip in the transverse setup using a $f = 250$ mm spherical lens. The outcoupled power was monitored over time while gradually increasing the laser power and has stayed stable for over three hours and intensities up to 2 MW/cm^2, suggesting no thermal or optomechanical damage.

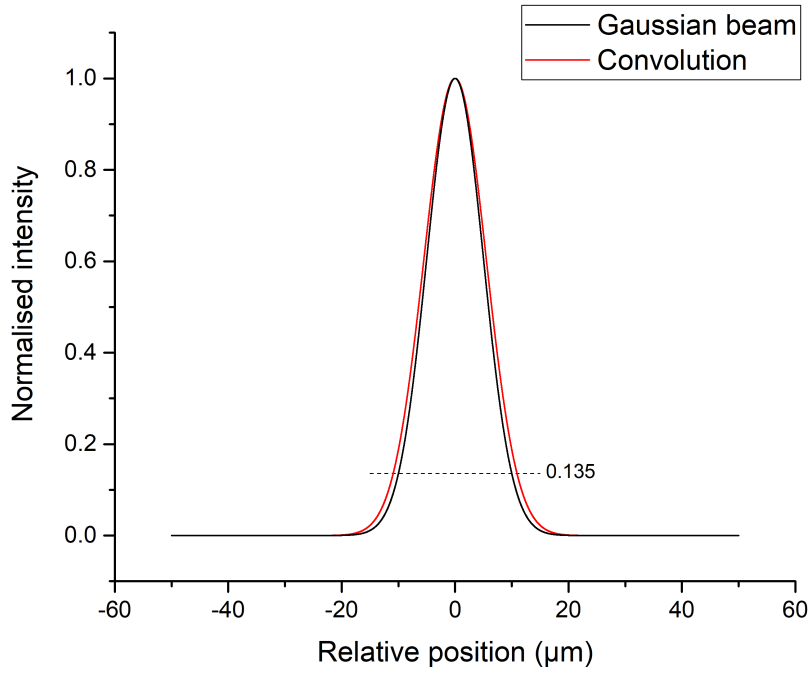

Figure 5.8: For a $w = 10\,\mu m$ wide Gaussian beam (black) and a 50 µm core fibre scanning the beam under a 10° angle, the convolution model (red curve) predicts an overestimate of the waist by about 1 µm. The dashed line marks the $1/e^2$ level where the waist is measured.

5.3.3 Vacuum profiling

The vacuum measurements were primarily focused on controlling and aligning the optical Bragg grating as described in Chapter 4, done with the same experimental setup and a single 50 µm core fibre. Using a $f = 250\,mm$ cylinder lens, the grating width was reliably measured and adjusted as needed over a period of several months without any observable change in beam profiles or measured intensities. This section describes additional testing of profiling capabilities at different powers up to 12 W, which would have been difficult to safely perform in air.

While the measurements performed in air have shown that increasing the amount of outcoupled light by increasing the core size barely broadens the beam at all, they were done at a constant laser power. To investigate the influence of the laser power itself, beam profiles were measured and compared starting at 12 W as measured directly in front of the vacuum chamber, gradually reducing the power via half-wave plate. The lowest power in this series was 130 mW. Figure 5.13 compares normalised 130 mW and 12 W profiles, showing virtually no difference between the two. All the features present in the higher power profile are mirrored and reliably reproduced, showing that all that is needed for successful profiling is some outcoupled light, even at such low intensities.

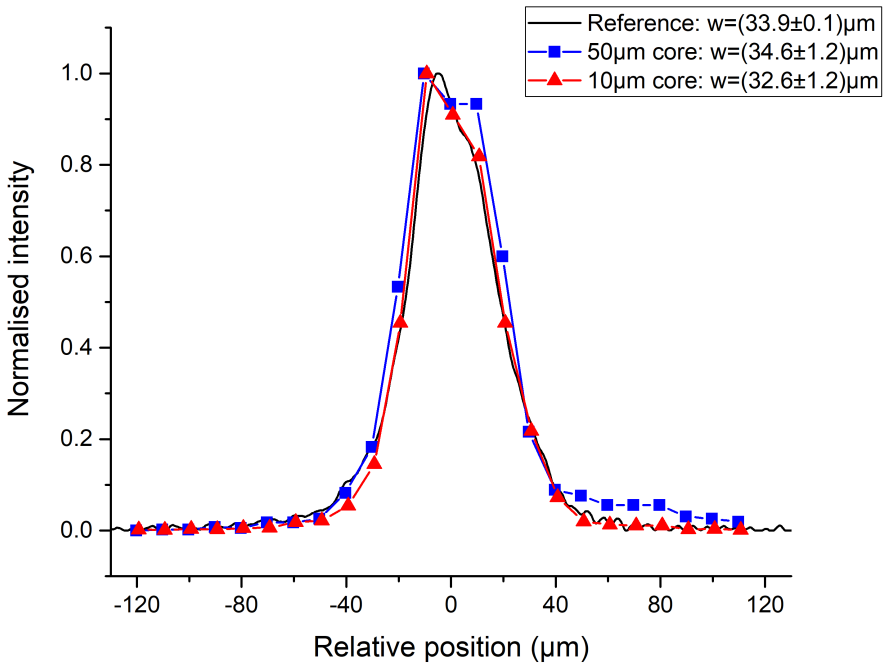

Figure 5.9: Comparison of transverse beam profiles measured using the moving edge profiler (reference, black), a 50 µm (blue) and 10 µm core fibre (red). The profiles were normalised and centred around zero for easier comparison. Both fibres reproduce the reference width well, deviating by less than 4%.

For tests at highest intensities the beam was focused to a 10 µm waist using a spherical $f = 250$ mm lens. Starting at 1.5 W power, the fibre was left in focus for 5 minutes, after which the beam profile was measured and the power gradually increased up to 12 W. During the measurements the polymer cladding was visibly outgassing, causing the pressure in the chamber to rapidly increase for a short while before dropping back to about 1×10^{-7} mbar. While this effect was visible for intensities above 200 kW/cm^2 and somewhat limits the high-vacuum compatibility, the pressure drops to background levels within a few minutes and can be avoided entirely by switching to fibres with glass cladding. Measured beam profiles and their corresponding widths, shown in Fig. 5.14, are measured consistently for up to 12 W. At this power, the profile distorts with waist increasing from 10 µm to 31(3) µm. All profiles measured afterwards were similarly distorted, suggesting that the tip had been irreversibly thermally damaged at an intensity above 4 MW/cm^2. Overall, fibre beam profiling is shown to be a reliable technique with micrometer resolution, even with moderate alignment and with significant durability even at high powers and in vacuum conditions. Even better resolution could be achieved by precisely aligning the fibre with respect to the beam axis, in principle resulting in a kernel bounded only by the roughness of the surface of the tip. Preparing extruded, pointed tips, although more involved than the approach described here, could potentially extend that to super-resolution below the laser wavelength.

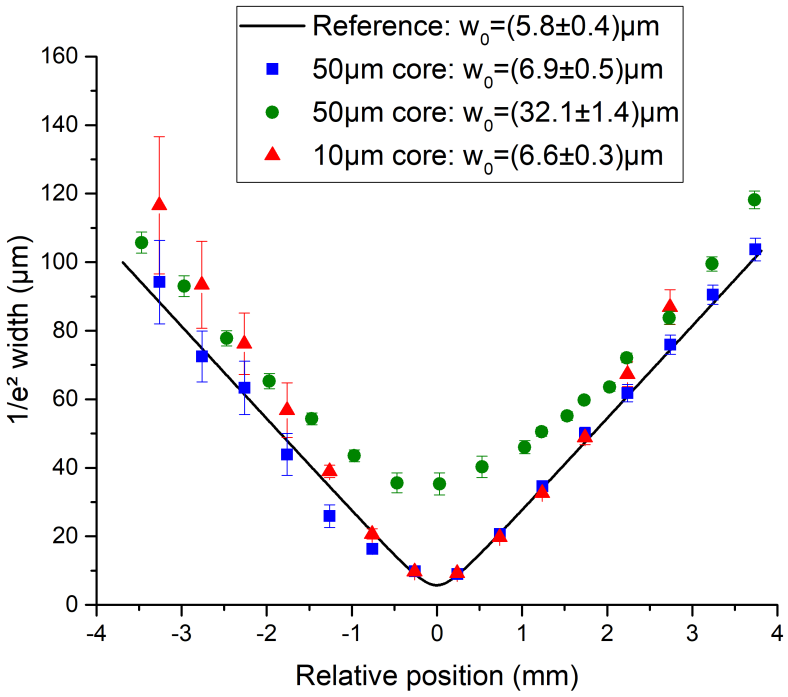

Figure 5.10: Comparison of extracted $1/e^2$ waists for transversely measured beam profiles. Fibre tips are placed in the xz plane and scanned along the x axis. The fitted reference profiler data (black curve) are well reproduced by the 10 µm core fibre (red triangles) and one of the two 50 µm core fibres (blue squares) used. The other 50 µm core (green circles) shows consistently higher values.

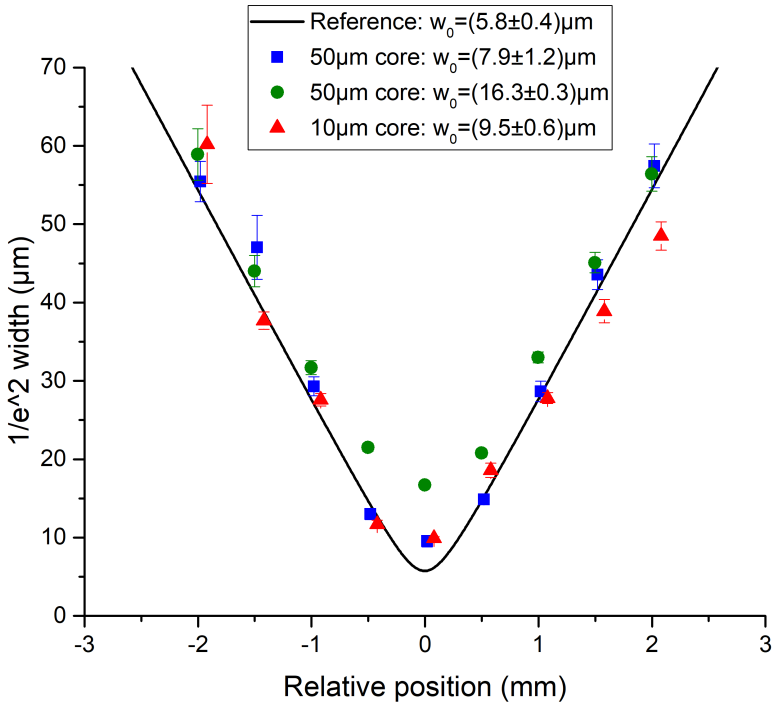

Figure 5.11: Comparison of longitudinal beam profiles' $1/e^2$ widths, measured for fibre tips in the yz-plane scanned along the x-axis. One of the 50 µm core tips (blue squares) and the 10 µm core tip show good agreement with fitted reference data by the moving edge profiler (black curve). The other 50 µm core tip overestimates the width, doing so consistently for all data points.

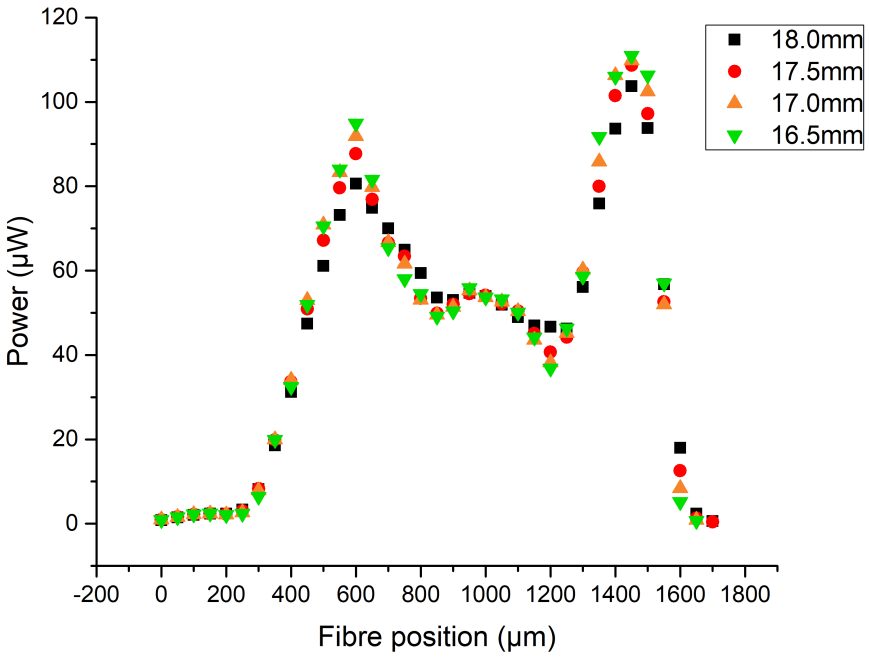

Figure 5.12: Beam profiles as measured using a 1000 µm core fibre over a 1.5 mm range of positions of the focusing lens. Unlike the smaller cores, the measured profiles are virtually identical and seemingly arbitrary, showing that the fibre's core should be comparable in size to the beam profile to obtain accurate results.

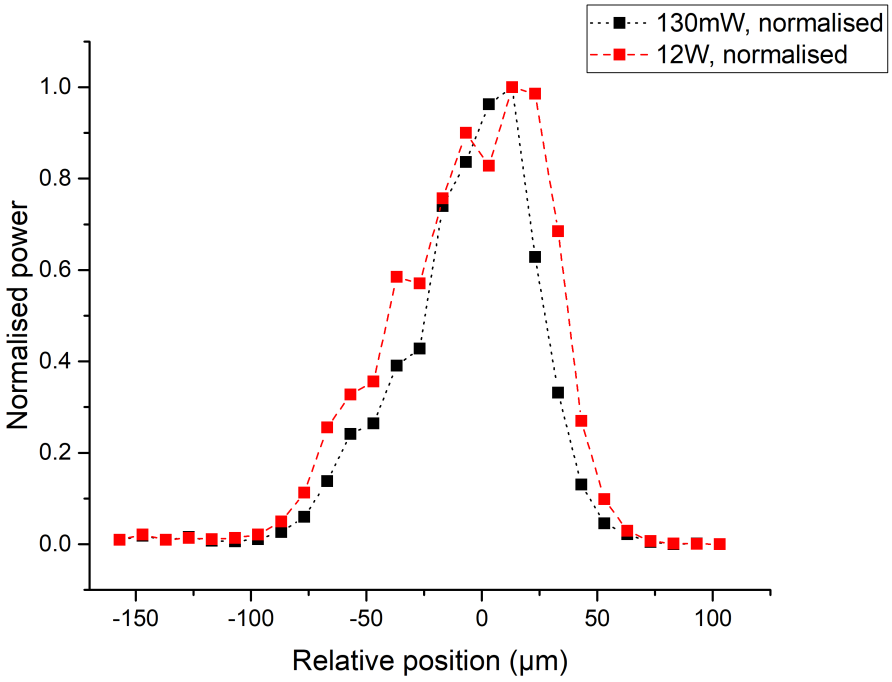

Figure 5.13: Normalised beam profiles obtained with a 10 µm core fibre in vacuum at 12 W (red) and 130 mW (black), as measured directly in front of the vacuum chamber.

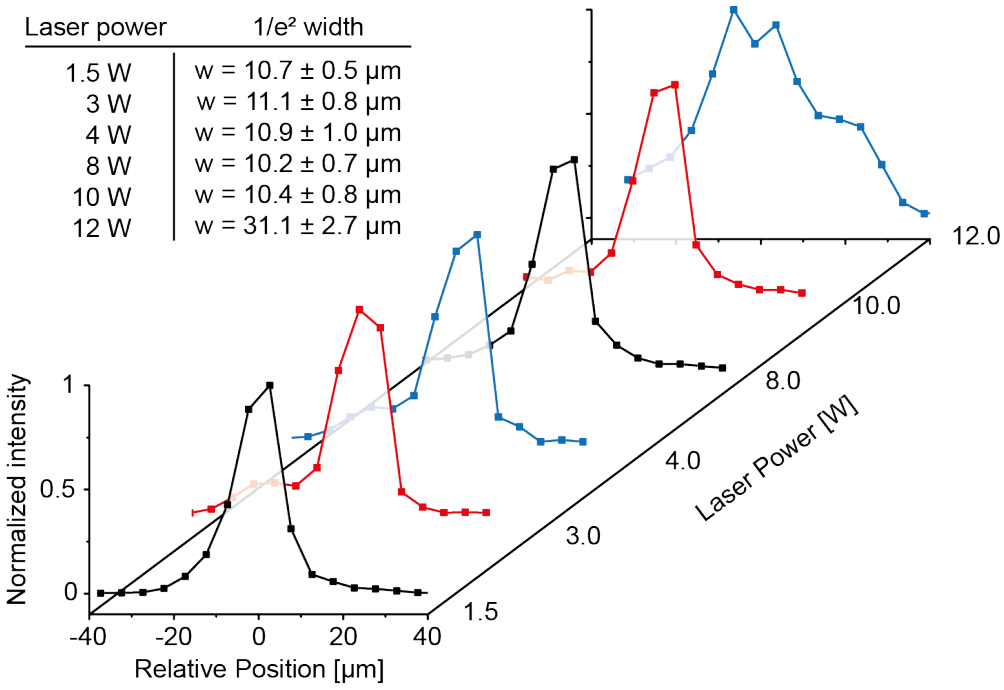

Figure 5.14: Beam profiles [77] measured with a 50 µm core fibre for laser powers up to 12 W. Sudden change in profile between 10 and 12 W suggests thermal degradation of the fibre tip for an intensity above 4 MW/cm^2.

6 Outlook

The presented Bragg diffraction experiments have demonstrated an equal-amplitude matter-wave beamsplitter and a roughly 70% efficient mirror, making an important step towards universal optical components for molecular quantum optics. While material nanomechanical gratings are often regarded as universal too, due to the basic diffraction mechanism being independent of the complexity and internal structure of the diffracted particle, they are not always advantageous for highly polarizable and polar molecules. Broadening of diffraction peaks and even loss of interference contrast are, for instance, observed when trying to diffract polar biomolecules on a dielectric silicon dioxide grating [61]. This effect, more pronounced for dielectric diffraction gratings, is explained through Casimir-Polder interaction of rotating electric dipoles with residual implanted charges from the grating manufacturing process, leading to a reduction and eventual loss in visibility dependent on the molecule's polarity, dipole moment and velocity. Similarly, dephasing of polar molecules can take place through van der Waals interactions with grating walls, but can be mitigated by using ultrathin gratings, where the molecule size and rotation period are comparable to the grating's thickness and the molecule's transit time [63].

Although thin optical and (ultra-)thin material gratings can be used for coherent beam splitting, the resulting splitting is not necessarily efficient since the incoming beam is split into several diffraction orders. Even in case of single-layer graphene grating [63], where all orders beside the first are suppressed, the beam is split into two on either side of the undiffracted peak. In contrast, Bragg diffraction demonstrates splitting into only two orders, demonstrating increased efficiency compared to selecting a single order of a multi-populated thin grating pattern. In addition, a desired momentum transfer and direction can be selected and tuned by varying the grating power and appropriately choosing the incidence angle, allowing for more versatile splitting compared to e.g. ultrathin material gratings.

The scheme can be further improved by prolonging the interaction time of molecules with the grating in order to strengthen the Bragg condition, hopefully resulting in sharper resonances and reduced losses to immediate diffraction orders. In practice, this could be achieved by either further spatially extending the grating or slowing down the molecules. Slowing could be realised, for instance, using buffer gas cells [94], letting molecules thermalise via collisions with low-density, cryogenic atomic gases. Furthermore, the coherence of the splitting could be confirmed by introducing a second Bragg grating recombining the molecular beam, which would, if successful, build an all-optical Mach Zehnder molecular interferometer. The framework and results of Bragg diffraction could also be extended towards realisation of Bloch oscillations on a moving standing light wave to obtain even larger momentum transfers.

Acknowledgments

First of all, I would like to thank my supervisor, Prof. Markus Arndt. Markus, thank you for giving me a chance to join your group and believing in me from early on, for all the invaluable advice and opportunities and the push I needed to take the leap into the unknown. I am deeply grateful for your continuous support and excited to see which direction the coming years are about to take our work in.

Another huge thanks goes to Dr. Christian Brand – for showing me the ropes in the lab and patiently answering all the questions I had and more, sometimes before I'd even thought of them. Thank you for all the tricks you have shown me, laughs shared during long hours in the lab, for all the feedback on this thesis, and most importantly, for helping me learn how to trust myself and setting me up to take over the experiment on my own.

In no small part thanks to all the *Molecoolis*, this past year has been nothing if not enjoyable. With someone always being there to lend a helping hand and with all the lunch discussions, cultivating our small plant family and endlessly throwing a plush bird around, I can only say I feel lucky and thankful to be working with such an amazing bunch that you all are. I would particularly like to thank Stephan for always having my back. Your advice and support have meant the world to me and I admire your dedication, diligence and calmness.

Last but not least, I am deeply indebted to my friends and family. The whirlwind that this past year has been would not have been possible without both the understanding of my friends for all the times when I was in the lab and their willingness to get me out of it for a much needed break. My deepest thanks goes to my family for supporting me every step of the way to get where I am today, both academically and by letting me branch out and explore my interests. Without knowing they will always be there to catch me if I fall, my mum's gentle reminders to sometimes stop and breathe and my dad remotely teaching me how to do bike and home repairs, all of this would have been much more difficult. Finally, I would like to thank my brother for sparking my curiosity in physics way back when I had no idea what a sine or a photon were, for all the Ljubljana and Prague breaks, for listening to (and understanding) all my frustrations about endless exams and experiments not wanting to be aligned, and being the best big brother I could have asked for.

Bibliography

[1] Louis De Broglie. Waves and Quanta. *Nature*, 112(2815):540–540, October 1923.

[2] G. P. Thomson and A. Reid. Diffraction of Cathode Rays by a Thin Film. *Nature*, 119(3007):890–890, June 1927.

[3] C. Davisson and L. H. Germer. Diffraction of Electrons by a Crystal of Nickel. *Physical Review*, 30(6):705–740, December 1927.

[4] H von Halbon and P Preiswerk. Preuve expérimentale de la diffraction des neutrons. *C. R. Acad. Sci Paris*, 203(735), 1936.

[5] H. Rauch, W. Treimer, and U. Bonse. Test of a single crystal neutron interferometer. *Physics Letters A*, 47(5):369–371, April 1974.

[6] Thomas H. Johnson. Photographic Record of First Order Diffraction of Hydrogen Atoms by a Lithium Fluoride Crystal. *Physical Review*, 35(10):1299–1300, May 1930.

[7] Ch. J. Bordé. Atomic interferometry with internal state labelling. *Physics Letters A*, 140(1):10–12, September 1989.

[8] O. Carnal and J. Mlynek. Young's double-slit experiment with atoms: A simple atom interferometer. *Physical Review Letters*, 66(21):2689–2692, May 1991.

[9] David W. Keith, Christopher R. Ekstrom, Quentin A. Turchette, and David E. Pritchard. An interferometer for atoms. *Physical Review Letters*, 66(21):2693–2696, May 1991.

[10] Mark Kasevich and Steven Chu. Atomic interferometry using stimulated Raman transitions. *Physical Review Letters*, 67(2):181–184, July 1991.

[11] I. Estermann and O. Stern. Beugung von Molekularstrahlen. *Zeitschrift für Physik*, 61(1):95–125, January 1930.

[12] Michael S. Chapman, Christopher R. Ekstrom, Troy D. Hammond, Richard A. Rubenstein, Jörg Schmiedmayer, Stefan Wehinger, and David E. Pritchard. Optics and Interferometry with Na_2 Molecules. *Physical Review Letters*, 74(24):4783–4786, June 1995. Publisher: American Physical Society.

[13] Markus Arndt, Olaf Nairz, Julian Vos-Andreae, Claudia Keller, Gerbrand van der Zouw, and Anton Zeilinger. Wave–particle duality of C 60 molecules. *Nature*, 401(6754):680–682, October 1999.

[14] Wieland Schöllkopf and J. Peter Toennies. Nondestructive Mass Selection of Small van der Waals Clusters. *Science*, 266(5189):1345–1348, November 1994.

[15] G. M. Tino and M. A. Kasevich. *Atom Interferometry*. International School of Physics 'Enrico Fermi'. IOS Press, Amsterdam, Netherlands, 2014. Issue: Course 188.

[16] Alexander D. Cronin, Jörg Schmiedmayer, and David E. Pritchard. Optics and interferometry with atoms and molecules. *Reviews of Modern Physics*, 81(3):1051–1129, July 2009.

[17] Paul Berman. *Atom Interferometry*. Elsevier, 1997.

[18] Antoine Browaeys, Thierry Lahaye, Trey Porto, Charles S. Adams, Matthias Weidemüller, and Leticia F. Cugliandolo, editors. *Current Trends in Atomic Physics*. Lecture Notes of the Les Houches Summer School. Oxford University Press, Oxford, New York, May 2019.

[19] Klaus Hornberger, Stefan Gerlich, Philipp Haslinger, Stefan Nimmrichter, and Markus Arndt. Colloquium: Quantum interference of clusters and molecules. *Reviews of Modern Physics*, 84(1):157–173, February 2012.

[20] R. Colella, A. W. Overhauser, and S. A. Werner. Observation of Gravitationally Induced Quantum Interference. *Physical Review Letters*, 34(23):1472–1474, June 1975.

[21] G. Rosi, F. Sorrentino, L. Cacciapuoti, M. Prevedelli, and G. M. Tino. Precision measurement of the Newtonian gravitational constant using cold atoms. *Nature*, 510(7506):518–521, June 2014.

[22] Achim Peters, Keng Yeow Chung, and Steven Chu. Measurement of gravitational acceleration by dropping atoms. *Nature*, 400(6747):849–852, August 1999.

[23] Peter Asenbaum, Chris Overstreet, Minjeong Kim, Joseph Curti, and Mark A. Kasevich. Atom-interferometric test of the equivalence principle at the 10^{-12} level. *arXiv:2005.11624 [gr-qc, physics:physics, physics:quant-ph]*, May 2020. arXiv: 2005.11624.

[24] David S. Weiss, Brenton C. Young, and Steven Chu. Precision measurement of the photon recoil of an atom using atomic interferometry. *Physical Review Letters*, 70(18):2706–2709, May 1993.

[25] Richard H. Parker, Chenghui Yu, Weicheng Zhong, Brian Estey, and Holger Müller. Measurement of the fine-structure constant as a test of the Standard Model. *Science*, 360(6385):191–195, April 2018.

[26] Yaakov Y. Fein, Philipp Geyer, Filip Kiałka, Stefan Gerlich, and Markus Arndt. Improved accuracy fullerene polarizability measurements in a long-baseline matter-wave interferometer. *Physical Review Research*, 1(3):033158, December 2019.

[27] Sandra Eibenberger, Xiaxi Cheng, J. P. Cotter, and Markus Arndt. Absolute Absorption Cross Sections from Photon Recoil in a Matter-Wave Interferometer. *Physical Review Letters*, 112(25):250402, June 2014.

[28] Yaakov Y. Fein, Armin Shayeghi, Lukas Mairhofer, Filip Kiałka, Philipp Rieser, Philipp Geyer, Stefan Gerlich, and Markus Arndt. Quantum-Assisted Measurement of Atomic Diamagnetism. *Physical Review X*, 10(1):011014, January 2020.

[29] A. Shayeghi, P. Rieser, G. Richter, U. Sezer, J. H. Rodewald, P. Geyer, T. J. Martinez, and M. Arndt. Matter-wave interference of a native polypeptide. *Nature Communications*, 11(1):1447, March 2020.

[30] Yaakov Y. Fein, Philipp Geyer, Patrick Zwick, Filip Kiałka, Sebastian Pedalino, Marcel Mayor, Stefan Gerlich, and Markus Arndt. Quantum superposition of molecules beyond 25 kDa. *Nature Physics*, 15(12):1242–1245, December 2019.

[31] Philip E. Moskowitz, Phillip L. Gould, Susan R. Atlas, and David E. Pritchard. Diffraction of an Atomic Beam by Standing-Wave Radiation. *Physical Review Letters*, 51(5):370–373, August 1983.

[32] Olaf Nairz, Björn Brezger, Markus Arndt, and Anton Zeilinger. Diffraction of Complex Molecules by Structures Made of Light. *Physical Review Letters*, 87(16):160401, September 2001.

[33] Stefan Gerlich, Lucia Hackermüller, Klaus Hornberger, Alexander Stibor, Hendrik Ulbricht, Michael Gring, Fabienne Goldfarb, Tim Savas, Marcel Müri, Marcel Mayor, and Markus Arndt. A Kapitza–Dirac–Talbot–Lau interferometer for highly polarizable molecules. *Nature Physics*, 3(10):711–715, October 2007.

[34] Philipp Haslinger, Nadine Dörre, Philipp Geyer, Jonas Rodewald, Stefan Nimmrichter, and Markus Arndt. A universal matter-wave interferometer with optical ionization gratings in the time domain. *Nature Physics*, 9(3):144–148, March 2013.

[35] Peter Martin, Bruce Oldaker, Andrew Miklich, and David Pritchard. Bragg scattering of atoms from a standing light wave. *Physical Review Letters*, 60(6):515–518, February 1988.

[36] Holger Müller, Sheng-wey Chiow, Quan Long, Sven Herrmann, and Steven Chu. Atom Interferometry with up to 24-Photon-Momentum-Transfer Beam Splitters. *Physical Review Letters*, 100(18):180405, May 2008.

[37] Tim Kovachy, Sheng-wey Chiow, and Mark A. Kasevich. Adiabatic-rapid-passage multiphoton Bragg atom optics. *Physical Review A*, 86(1):011606, July 2012.

[38] Maxime Ben Dahan, Ekkehard Peik, Jakob Reichel, Yvan Castin, and Christophe Salomon. Bloch Oscillations of Atoms in an Optical Potential. *Physical Review Letters*, 76(24):4508–4511, June 1996.

[39] Chenghui Yu, Weicheng Zhong, Brian Estey, Joyce Kwan, Richard H. Parker, and Holger Müller. Atom-Interferometry Measurement of the Fine Structure Constant. *Annalen der Physik*, 531(5):1800346, 2019.

[40] Martina Gebbe, Sven Abend, Jan-Niclas Siemß, Matthias Gersemann, Holger Ahlers, Hauke Müntinga, Sven Herrmann, Naceur Gaaloul, Christian Schubert, Klemens Hammerer, Claus Lämmerzahl, Wolfgang Ertmer, and Ernst M. Rasel. Twin-lattice atom interferometry. *arXiv:1907.08416 [physics, physics:quant-ph]*, July 2019. arXiv: 1907.08416.

[41] T. Kovachy, P. Asenbaum, C. Overstreet, C. A. Donnelly, S. M. Dickerson, A. Sugarbaker, J. M. Hogan, and M. A. Kasevich. Quantum superposition at the half-metre scale. *Nature*, 528(7583):530–533, December 2015.

[42] Thomas Young. The Bakerian Lecture: On the Theory of Light and Colours. *Philosophical Transactions of the Royal Society of London*, 92:12–48, 1802.

[43] Thomas Young. *A course of lectures on natural philosophy and the mechanical arts*, volume 1. Printed for J. Johnson, London, 1807.

[44] G. Kirchhoff. Zur Theorie der Lichtstrahlen. *Annalen der Physik*, 254(4):663–695, 1883.

[45] E. Wigner. On the Quantum Correction For Thermodynamic Equilibrium. *Physical Review*, 40(5):749–759, June 1932.

[46] Justin Peatross and Michael Ware. *Physics of Light and Optics*. Available online at optics.buy.edu, 2015 edition, April 2019.

[47] J. E. Moyal. Quantum mechanics as a statistical theory. *Mathematical Proceedings of the Cambridge Philosophical Society*, 45(1):99–124, January 1949.

[48] Wolfgang P. Schleich. *Quantum Optics in Phase Space*. Wiley-VCH, 2001.

[49] Thomas Juffmann. The Wigner Function: A phase-space description for matter waves, May 2019.

[50] William B. Case. Wigner functions and Weyl transforms for pedestrians. *American Journal of Physics*, 76(10):937–946, September 2008.

[51] Klaus Hornberger, Stefan Gerlich, Hendrik Ulbricht, Lucia Hackermüller, Stefan Nimmrichter, Ilya V Goldt, Olga Boltalina, and Markus Arndt. Theory and experimental verification of Kapitza–Dirac–Talbot–Lau interferometry. *New Journal of Physics*, 11(4):043032, April 2009.

[52] Dieter Meschede. *Optik, Licht und Laser*. Vieweg+Teubner, 3 edition, 2008.

[53] Daniel A. Steck. Classical and modern optics. Available online at `http://steck.us/teaching`, February 2020. Revision 1.7.6, 20 February 2020.

[54] Christopher J. Foot. *Atomic Physics*. Oxford master series in physics. Oxford University Press, 2005.

[55] Alan Corney. *Atomic and Laser Spectroscopy*. Clarendon Press [u.a.], Oxford, 1977.

[56] Klaus Hornberger, John E. Sipe, and Markus Arndt. Theory of decoherence in a matter wave Talbot-Lau interferometer. *Physical Review A*, 70(5):053608, November 2004.

[57] Michael S. Chapman, Troy D. Hammond, Alan Lenef, Jörg Schmiedmayer, Richard A. Rubenstein, Edward Smith, and David E. Pritchard. Photon Scattering from Atoms in an Atom Interferometer: Coherence Lost and Regained. *Physical Review Letters*, 75(21):3783–3787, November 1995.

[58] David A. Kokorowski, Alexander D. Cronin, Tony D. Roberts, and David E. Pritchard. From Single- to Multiple-Photon Decoherence in an Atom Interferometer. *Physical Review Letters*, 86(11):2191–2195, March 2001.

[59] Lucia Hackermüller, Klaus Hornberger, Björn Brezger, Anton Zeilinger, and Markus Arndt. Decoherence of matter waves by thermal emission of radiation. *Nature*, 427(6976):711–714, February 2004.

[60] J. P. Cotter, S. Eibenberger, L. Mairhofer, X. Cheng, P. Asenbaum, M. Arndt, K. Walter, S. Nimmrichter, and K. Hornberger. Coherence in the presence of absorption and heating in a molecule interferometer. *Nature Communications*, 6(1):7336, June 2015.

[61] Christian Knobloch, Benjamin A. Stickler, Christian Brand, Michele Sclafani, Yigal Lilach, Thomas Juffmann, Ori Cheshnovsky, Klaus Hornberger, and Markus Arndt. On the role of the electric dipole moment in the diffraction of biomolecules at nanomechanical gratings. *Fortschritte der Physik*, 65(6-8):1600025, 2017.

[62] Christian Brand, Johannes Fiedler, Thomas Juffmann, Michele Sclafani, Christian Knobloch, Stefan Scheel, Yigal Lilach, Ori Cheshnovsky, and Markus Arndt. A Green's function approach to modeling molecular diffraction in the limit of ultra-thin gratings. *Annalen der Physik*, 527(9-10):580–591, 2015.

[63] Christian Brand, Michele Sclafani, Christian Knobloch, Yigal Lilach, Thomas Juffmann, Jani Kotakoski, Clemens Mangler, Andreas Winter, Andrey Turchanin, Jannik Meyer, Ori Cheshnovsky, and Markus Arndt. An atomically thin matter-wave beamsplitter. *Nature Nanotechnology*, 10(10):845–848, October 2015.

[64] Michele Sclafani, Thomas Juffmann, Christian Knobloch, and Markus Arndt. Quantum coherent propagation of complex molecules through the frustule of the alga *Amphipleura pellucida*. *New Journal of Physics*, 15(8):083004, August 2013.

[65] Christian Brand, Filip Kiałka, Stephan Troyer, Christian Knobloch, Ksenija Simonović, Benjamin A. Stickler, Klaus Hornberger, and Markus Arndt. Bragg diffraction of large organic molecules. *In print*, 2020.

[66] Alexander Franzen. Component library: a vector graphics library for illustrations of optics experiments. `http://www.gwoptics.org/ComponentLibrary/`, 2006. Available under a Creative Commons CC BY-NC 3.0 licence.

[67] Christian Knobloch. *Coherent matter-wave manipulation techniques*. PhD thesis, University of Vienna, Vienna, Austria, 2019.

[68] Jeetendra Bhawsar. Computational Study of Corrosion Potential of Ciprofloxacin Drug: DFT Approach. *Asian J. Research Chem.*, 07:386–389, April 2014.

[69] R. Ramprasad and N. Shi. Polarizability of phthalocyanine based molecular systems: A first-principles electronic structure study. *Applied Physics Letters*, 88(22):222903, May 2006.

[70] Hai Du, Ru-Chun Amy Fuh, Junzhong Li, L. Andrew Corkan, and Jonathan S. Lindsey. PhotochemCAD: A Computer-Aided Design and Research Tool in Photochemistry. *Photochemistry and Photobiology*, 68(2):141–142, 1998.

[71] Chia-Chang Lin and Min-Shan Wu. Degradation of ciprofloxacin by UV/S2O82 process in a large photoreactor. *Journal of Photochemistry and Photobiology A: Chemistry*, 285:1–6, July 2014.

[72] Sonia Carabineiro, Adrián Silva, Cláudia Silva, Ricardo Segundo, Goran Dražić, José Figueiredo, and Joaquim Faria. Titanium Dioxide–Based Materials for Photocatalytic Conversion of Water Pollutants. pages 247–269. December 2014.

[73] Asad Muhammad Khan and Syed Sakhawat Shah. Fluorescence Spectra Behavior of Ciprofloxacin HCl in Aqueous Medium and Its Interaction with Sodium Dodecyl Sulfate. *Journal of Dispersion Science and Technology*, 30(7):997–1002, July 2009.

[74] Thomas Juffmann, Adriana Milic, Michael Müllneritsch, Peter Asenbaum, Alexander Tsukernik, Jens Tüxen, Marcel Mayor, Ori Cheshnovsky, and Markus Arndt. Real-time single-molecule imaging of quantum interference. *Nature Nanotechnology*, 7(5):297–300, May 2012.

[75] Joseph P. Cotter, Christian Brand, Christian Knobloch, Yigal Lilach, Ori Cheshnovsky, and Markus Arndt. In search of multipath interference using large molecules. *Science Advances*, 3(8):e1602478, August 2017.

[76] Stephan Troyer. Diffraction and biological detection of the antibiotic ciprofloxacin. Master's thesis, University of Vienna, Vienna, Austria, 2019.

[77] Christian Brand, Ksenija Simonović, Filip Kiałka, Stephan Troyer, Philipp Geyer, and Markus Arndt. A fiber-based beam profiler for high-power laser beams in confined spaces and ultra-high vacuum. *Optics Express*, 28(5):6164, March 2020.

[78] William Henry Bragg and William Lawrence Bragg. The reflection of X-rays by crystals. *Proceedings of the Royal Society of London. Series A, Containing Papers of a Mathematical and Physical Character*, 88(605):428–438, July 1913.

[79] E. I. Gordon. A Review of Acoustooptical Deflection and Modulation Devices. *Applied Optics*, 5(10):1629–1639, October 1966.

[80] K. O. Hill, B. Malo, F. Bilodeau, D. C. Johnson, and J. Albert. Bragg gratings fabricated in monomode photosensitive optical fiber by UV exposure through a phase mask. *Applied Physics Letters*, 62(10):1035–1037, March 1993.

[81] G. A. Ball and W. W. Morey. Compression-tuned single-frequency Bragg grating fiber laser. *Optics Letters*, 19(23):1979–1981, December 1994.

[82] Fengqin Huang, Tao Chen, Jinhai Si, Xuantung Pham, and Xun Hou. Fiber laser based on a fiber Bragg grating and its application in high-temperature sensing. *Optics Communications*, 452:233–237, December 2019.

[83] D. Sippel, K. Kleinstück, and G. E. R. Schulze. Neutron diffraction of ideal crystals using a double crystal spectrometer. *Physics Letters*, 8(4):241–242, February 1964.

[84] D. Sippel, K. Kleinstück, and G. E. R. Schulze. Pendellösungs-Interferenzen mit thermischen Neutronen an Si-Einkristallen. *Physics Letters*, 14(3):174–175, February 1965.

[85] C. G. Shull. Observation of Pendellösung Fringe Structure in Neutron Diffraction. *Physical Review Letters*, 21(23):1585–1589, December 1968. Publisher: American Physical Society.

[86] Sheng-wey Chiow, Tim Kovachy, Hui-Chun Chien, and Mark A. Kasevich. $102\,\hbar k$ Large Area Atom Interferometers. *Physical Review Letters*, 107(13):130403, September 2011. Publisher: American Physical Society.

[87] G. Rosi, G. D'Amico, L. Cacciapuoti, F. Sorrentino, M. Prevedelli, M. Zych, Č Brukner, and G. M. Tino. Quantum test of the equivalence principle for atoms in coherent superposition of internal energy states. *Nature Communications*, 8(1):15529, June 2017.

[88] Chris Overstreet, Peter Asenbaum, Tim Kovachy, Remy Notermans, Jason M. Hogan, and Mark A. Kasevich. Effective Inertial Frame in an Atom Interferometric Test of the Equivalence Principle. *Physical Review Letters*, 120(18):183604, May 2018.

[89] Claudia Keller. *Bewegung von Atomen in starken Lichtfeldern*. PhD thesis, University of Vienna, Vienna, Austria, October 1999.

[90] C. Keller, J. Schmiedmayer, A. Zeilinger, T. Nonn, S. Dürr, and G. Rempe. Adiabatic following in standing-wave diffraction of atoms. *Applied Physics B*, 69(4):303–309, October 1999.

[91] Holger Mueller, Sheng-wey Chiow, and Steven Chu. Atom-wave diffraction between the Raman-Nath and the Bragg regime: Effective Rabi frequency, losses, and phase shifts. *Physical Review A*, 77(2):023609, February 2008. arXiv: 0704.2627.

[92] Bastian Schwarz, Gunnar Ritt, Michael Koerber, and Bernd Eberle. Laser-induced damage threshold of camera sensors and micro-optoelectromechanical systems. *Optical Engineering*, 56(3):034108, March 2017.

[93] Gaussian beam waist illustration. Wikipedia Commons, available under CC-BY-SA 3.0.

[94] Julia Piskorski, David Patterson, Sandra Eibenberger, and John M. Doyle. Cooling, Spectroscopy and Non-Sticking of trans-Stilbene and Nile Red. *ChemPhysChem*, 15(17):3800–3804, December 2014.